MNRAS 000, 1–13 (0000) Preprint 22 April 2021 Compiled using MNRAS LATEX style file v3.0

Where Outflows Meet Inflows: Gas Kinematics in SSA22 Lyman-α Blob 2 Decoded by Advanced Radiative Transfer Modelling

Zhihui Li,[1]⋆ Charles C. Steidel,[1] Max Gronke[2]†, Yuguang Chen[1] and Yuichi Matsuda[3,4]
[1]Cahill Center for Astrophysics, California Institute of Technology, MC 249-17, 1200 East California Boulevard, Pasadena, CA 91125, USA
[2]Department of Physics & Astronomy, Johns Hopkins University, Baltimore, MD 21218, USA
[3]National Astronomical Observatory of Japan, 2-21-1 Osawa, Mitaka, Tokyo 181-8588, Japan
[4]Department of Astronomy, School of Science, The Graduate University for Advanced Studies, SOKENDAI, Osawa, Mitaka, Tokyo 181-8588, Japan

ABSTRACT

We present new spectroscopic observations of Lyman-α (Lyα) Blob 2 (LAB2) in the SSA22 protocluster region ($z \sim 3.1$). By creating a narrow-band Lyα image, we observed extended Lyα emission in three distinct regions, in which the highest Lyα surface brightness (SB) center is far away from the known continuum sources. We have searched through the MOSFIRE slits that cover the high Lyα SB regions, but are unable to detect any significant nebular emission near the highest SB center. We further map the blue-to-red flux ratio and find that it is anti-correlated with Lyα SB with a power-law index of ~ -0.4. To decode the spatially-resolved Lyα profiles using Monte-Carlo radiative transfer (MCRT) modelling, we use both multiphase, clumpy models and shell models and successfully reproduced the diverse Lyα morphologies with reasonable physical parameters. Significant correlations exist between parameters of two different models, and our multiphase, clumpy model parameters naturally alleviated the previously reported discrepancies between the shell model parameters and data. In addition, we have modeled Lyα spectra at different spatial positions simultaneously, and we find that the variation of the inferred clump outflow velocity can be approximately explained by line-of-sight projection effects. Our results support the 'central powering + scattering' scenario, i.e. the Lyα photons are generated by a central powering source and then scatter with outflowing, multiphase H I gas while propagating outwards. The infalling of cool gas near the blob outskirts shapes the observed blue-dominated Lyα profiles, but its energy contribution is likely to be minor compared to the photo-ionization by star-forming galaxies and/or AGNs.

Key words: galaxies: kinematics and dynamics — intergalactic medium — galaxies: high-redshift — galaxies: evolution

1 INTRODUCTION

Lyman-α blobs (LABs) – spatially extended (projected sizes $\gtrsim 100$ kpc) gaseous nebulae with tremendous Lyα luminosities ($L_{\rm Ly\alpha} \sim 10^{43-44}\,{\rm erg\,s^{-1}}$) seen at high redshifts ($z \gtrsim 2$) – are among the most mysterious and intriguing objects in the universe. Thus far, numerous LABs have been discovered via narrow-band imaging or in galaxy surveys (e.g. Francis et al. 1996; Fynbo et al. 1999; Keel et al. 1999; Steidel et al. 2000; Matsuda et al. 2004, 2011; Dey et al. 2005; Saito et al. 2006; Smith & Jarvis 2007; Hennawi et al. 2009; Ouchi et al. 2009; Prescott et al. 2009, 2012; Erb et al. 2011; Cai et al. 2017), yet their physical origin remains obscure. It is found that LABs are preferentially located in overdense proto-cluster regions, which are expected to be the progenitors of the massive galaxy clusters observed today (e.g. Steidel et al. 1998; Prescott et al. 2008; Yang et al. 2009, 2010; Hine et al. 2016a). Therefore, the study of LABs may illuminate the formation and evolution of massive galaxies and the mechanisms of associated feedback events.

Up to now, many hypotheses about the powering mechanisms of LABs have been proposed, including: (1) photo-ionization by central energetic sources (starburst galaxies or AGNs, see e.g. Haiman & Rees 2001; Cantalupo et al. 2005, 2014). This scenario gained credence from infrared and submillimeter observations that discovered luminous galaxies and AGNs associated with some LABs (Chapman et al. 2001; Dey et al. 2005; Geach et al. 2005, 2007, 2009; Colbert et al. 2006; Webb et al. 2009). (2) Starburst-induced, shock-powered galactic-wide outflows ('superwinds', see e.g. Heckman et al. 1990; Taniguchi & Shioya 2000; Taniguchi et al. 2001; Mori et al. 2004). This scenario has been corroborated by the observed redward asymmetric Lyα profiles (Dawson et al. 2002; Ajiki et al. 2002) and shell-like or bubble-like structures (Matsuda et al. 2004; Wilman et al. 2005). (3) Gravitational cooling radiation from accretion of cold gas streams onto protogalaxies (e.g. Haiman et al. 2000; Fardal et al. 2001; Furlanetto et al. 2005; Dijkstra et al. 2006a,b; Goerdt et al. 2010; Faucher-Giguère et al. 2010; Rosdahl & Blaizot 2012). This scenario may be preferred for LABs that appear to lack powerful sources despite deep multi-wavelength observations and exhibit blueward asymmetric Lyα profiles (Nilsson et al. 2006; Smith & Jarvis 2007; Saito et al. 2008; Smith et al. 2008; Daddi et al. 2020). (4) Resonant scattering of Lyα photons (e.g. Dijkstra & Loeb 2008; Steidel et al. 2010, 2011). As resonant scattering imposes polarization, recent polarimetric observations and simulations have provided evidence of scattering within LABs, albeit with remaining uncertainties (Dijkstra & Loeb 2009; Hayes et al. 2011; Beck et al. 2016; Trebitsch et al. 2016; Eide et al. 2018; Kim et al. 2020).

To further distinguish these different powering mechanisms, it is beneficial to study spatially-resolved Lyα spectra, which are made possible by the outstanding capabilities of recently commissioned integral field unit (IFU) spectrographs, such as KCWI (Keck Cosmic Web Imager, Morrissey et al. 2018) and MUSE (Multi Unit Spectroscopic Explorer, Bacon et al. 2014). These instruments have revolutionized the study of extended Lyα nebulae by adding an additional spatial dimension with unprecedented sensitivity at rest-frame UV wavelengths (see e.g. Wisotzki et al. 2016; Leclercq et al. 2017, 2020).

In this paper, we present new KCWI observations of one of the giant LABs discovered in the overdense proto-cluster region SSA22 at $z \sim 3.1$, SSA22-Blob2 (LAB2, Steidel et al. 1998, 2000). LAB2 has an immense Lyα luminosity of $\sim 10^{44}\,{\rm erg\,s^{-1}}$ and a spatial extent of ~ 100 kpc. Ever since its discovery, LAB2 has become the target of many follow-up observations at multiple wavelengths, including X-ray (Basu-Zych & Scharf 2004; Geach et al. 2009; Lehmer et al. 2009a,b), optical (Wilman et al. 2005; Martin et al. 2014), infrared (IR, Geach et al. 2007; Webb et al. 2009), and submillimeter (submm, Chapman et al. 2001; Hine et al. 2016b). A Lyman-break galaxy (LBG), M14 (Steidel et al. 2000), and an X-

⋆ E-mail: zhihui@caltech.edu
† Hubble fellow

ray source (Basu-Zych & Scharf 2004) have been identified within LAB2.

To analyse the spatially-resolved Lyα profiles obtained by KCWI, we carried out Monte-Carlo radiative transfer (MCRT) modelling assuming a multiphase, clumpy H I gas model. As a presumably realistic description of the H I gas in the interstellar medium (ISM) and the circumgalactic medium (CGM), the multiphase, clumpy model has been explored by many theoretical studies (e.g. Neufeld 1991; Hansen & Oh 2006; Dijkstra & Kramer 2012; Laursen et al. 2013; Gronke & Dijkstra 2016). Observationally, Li et al. (2021) made the first successful attempt to systemically fit the spatially-resolved Lyα profiles with the multiphase, clumpy model. The present work is a direct follow-up of Li et al. (2021), exploring a different parameter space with new physical interpretation of the derived parameters.

The structure of this paper is as follows. In §2, we describe our KCWI and MOSFIRE observations and data reduction procedures. In §3, we present the spatial distribution and spectral profiles of Lyα emission. In §4, we present the non-detection of nebular emission within LAB2 with MOSFIRE. In §5, we detail the methodology and present the results of radiative transfer modelling using the multiphase, clumpy model. In §6, we summarize previous studies of LAB2 and compare with this work. In §7, we summarize and conclude. Throughout this paper we adopt a flat ΛCDM cosmology with $\Omega_{\rm m} = 0.315$, $\Omega_\Lambda = 0.685$, and $H_0 = 67.4$ km s^{-1} Mpc^{-1} (Planck Collaboration et al. 2018). We use the following vacuum wavelengths: 1215.67 Å for Lyα, 4862.683 Å for Hβ, and 4960.295/5008.240 Å for [O III] from the Atomic Line List v2.04[1].

2 OBSERVATIONS AND DATA REDUCTION

2.1 KCWI Observations

The KCWI observations of LAB2 were carried out on the night of 2019 September 27, with a seeing of $\sim 0.4-0.5''$ full width at half maximum (FWHM). We used the KCWI large slicer, which provides a contiguous field-of-view of $20.4''$ (slice length) $\times$ $33''$ ($24 \times 1.35''$ slice width). With the BM VPH grating set up for $\lambda_{\rm c} = 4800$ Å, the wavelength coverage is $\sim 4260-5330$ Å, with spectral resolution $R \simeq 1800-2200$. The data were obtained as 8 individual 1200 s exposures, with small telescope offsets in the direction perpendicular to slices applied between each, in an effort to recover some spatial resolution given the relatively large slice width. The total on-source exposure time was 2.7 hours.

Individual exposures were reduced using the KCWI Data Reduction Pipeline[2], which includes wavelength calibration, atmospheric refraction correction, background subtraction, and flux calibration. The individual datacubes were then spatially re-sampled onto a uniform astrometric grid with $0.3''$ by $0.3''$ spaxels, with a sampling of 0.5 Å pix^{-1} (4.75 pixels per spectral resolution element) along the wavelength axis, using a variant of the 'drizzle' algorithm (with a drizzle factor of 0.9) in the `MONTAGE`[3] package. The re-sampled cubes were then combined into a final stacked cube by averaging with exposure time weighting. Owing to the coarser spatial sampling in the long dimension of the spatial cube, the PSF in the final datacube is elongated along the N-S direction, with FWHM $\simeq 0.90'' \times 1.08''$ (X-direction and Y-direction, respectively) measured from the most compact object in the field.

The resampled final datacube covers a scientifically useful solid angle of $22.6'' \times 33.6''$ on the sky, and a wavelength range (vacuum, heliocentric) of 4214 – 5243 Å. A variance image with the same dimensions was created by propagating errors based on a noise model throughout the data reduction.

[1] http://www.pa.uky.edu/~peter/atomic/index.html
[2] https://github.com/Keck-DataReductionPipelines/KcwiDRP
[3] http://montage.ipac.caltech.edu

Table 1. MOSFIRE *K*-band observations of LAB2.

Name	Width	R	PA	Exp	Seeing	Date of Obs	Nod
(1)	(2)	(3)	(4)	(5)	(6)	(7)	(8)
Slit 1	1.0	2660	−54.0	2.0	0.71	2020 Nov 27	±20.0
Slit 2	1.0	2660	−54.0	2.5	0.45	2019 Jun 15	±15.0

Notes. The details of the MOSFIRE *K*-band observations of LAB2. The columns are: (1) slit name; (2) slit width ($''$); (3) resolving power ($\lambda/\Delta\lambda$); (4) slit PA (degrees E of N); (5) exposure time in hours; (6) seeing FWHM ($''$); (7) UT date of observation; (8) nod amplitude between A and B positions ($''$).

Table 2. Continuum sources identified in LAB2.

Name	RA (J2000)	Dec (J2000)	$z_{\rm sys}$	Type	Refs.
M14[a]	22:17:39.09	+00:13:29.8	3.091	Lyα	(1)(2)
LAB2-a	22:17:39.3	+00:13:22.0	...	IR	(3)
LAB2-b	22:17:39.1	+00:13:30.7	...	IR	(3)
LAB2-ALMA	22:17:39.079	+00:13:30.85	...	Submm	(4)
LAB2-X-ray	22:17:39.08	+00:13:30.7	...	X-ray	(5)

[a]Originally defined in Steidel et al. (2000).
Notes. Properties of the continuum sources identified in LAB2. The columns are: (1) name of the source; (2) right ascension; (3) declination; (4) systemic redshift; (5) type of observation; (6) references.
References. (1) Steidel et al. (2003); (2) Nestor et al. (2013); (3) Webb et al. (2009); (4) Ao et al. (2017); (5) Lehmer et al. (2009a).

2.2 MOSFIRE Observations

We observed selected regions of LAB2, chosen to include the highest Lyα surface brightness areas, using MOSFIRE (McLean et al. 2010, 2012; Steidel et al. 2014) on the Keck I telescope. Spectra in the near-IR *K* band (1.967 – 2.393 μm) were obtained using two slitmasks with the same sky PA, which cover two parallel regions of width $1''$ separated by $0.25''$ on the sky, as shown in Figure 1 and summarised in Table 1. Slit 1 passes through the region with the highest Lyα surface brightness (labeled 11 in Fig. 1), while Slit 2 abuts that region immediately to the south, and also includes a second high SB region (labeled 13) to the southeast.

The MOSFIRE observations of Slit 1 and Slit 2 were obtained on two separate observing runs, both under clear conditions with sub-arcsec seeing. With $1.0''$ slits in the *K* band, MOSFIRE achieves a spectral resolving power $R \sim 2660$. The data were taken with the MOSFIRE "masknod" mode, using two telescope positions separated by $30-40''$ along the slit direction, with individual exposures of 180 s between nods. The total integration times were 2.0 hours for Slit 1 and 2.5 hours for Slit 2. The data for each observation sequence were reduced using the MOSFIRE data reduction pipeline[4] to produce two-dimensional, rectified, background-subtracted vacuum wavelength calibrated spectrograms (see Steidel et al. 2014 for details). Observations obtained on different observing nights using the same slitmask were reduced independently; the 2-D spectrograms were shifted into the heliocentric rest frame and combined with inverse variance weighting using tasks in the `MOSPEC` (Strom et al. 2017) analysis package.

3 Lyα EMISSION IN LAB2

3.1 Spatial Distribution of Lyα Emission

To provide an overview of the Lyα surface brightness (SB) distribution in LAB2, we first generated a Lyα narrow-band image by summing all the Lyα fluxes over the relevant wavelength range. Similar to Li et al. (2021), we followed the 'matched filtering' procedures using `LSDCat` (Herenz & Wisotzki 2017), specifically with three steps: (1) applying spatial filtering to the spatially (3 pixel $\times$ 3 pixel boxcar) and spectrally (σ = 0.5 Å Gaussian) smoothed

[4] https://github.com/Keck-DataReductionPipelines/MosfireDRP

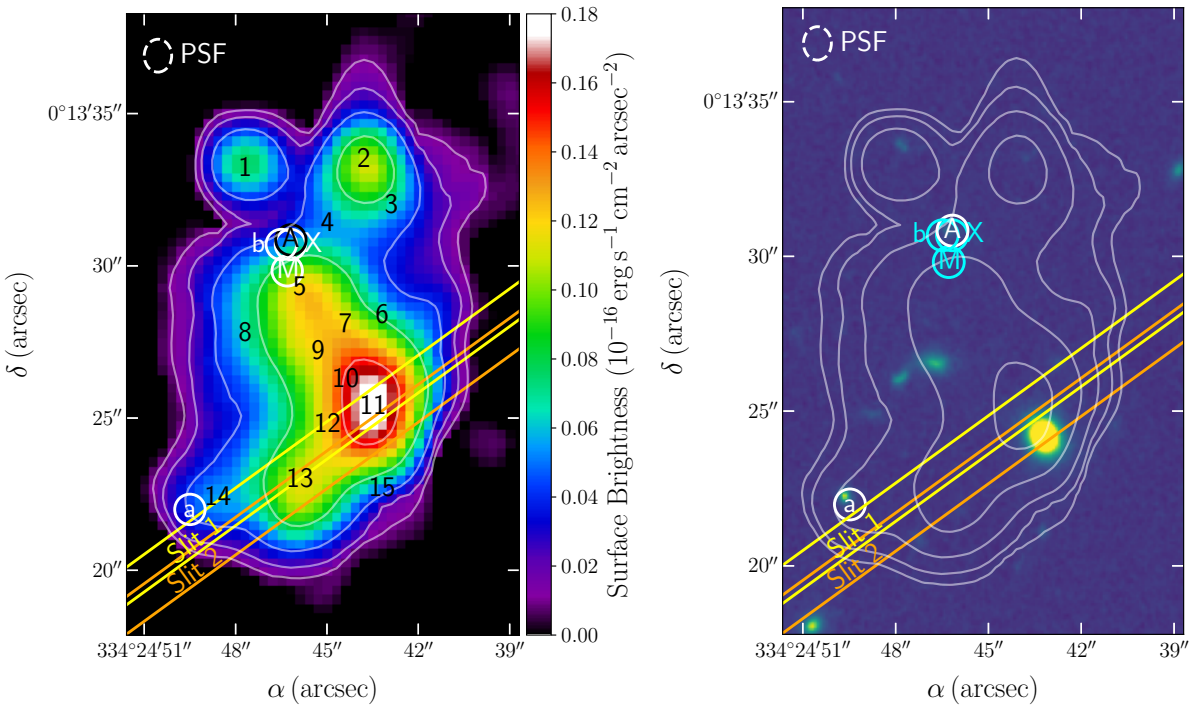

Figure 1. Lyα and continuum images of LAB2. *Left*: The narrow band Lyα image, obtained by collapsing the original KCWI datacube over 4949 – 5009 Å, which encloses the Lyα line (see §3.1). The UV continuum near the wavelength of Lyα has been subtracted. The positions of the MOSFIRE slits are delineated by parallel yellow and orange lines (see §2.2), and the numbers (1-15, in black) indicate the positions of spectra that we sample for radiative transfer modelling in §5. *Right*: The *HST* WFC3-IR F160W rest-frame optical continuum image. The positions of a Lyman-break galaxy (M14, labeled as 'M'), an X-ray source (labeled as 'X') with IR ('b') and submm ('A') counterparts, and an IR source ('a') have been marked on each image (see §3.2 and Table 2). The Lyα isophotes with levels of $\mathrm{SB_{Ly\alpha}} = [150, 80, 40, 20, 10] \times 10^{-19}$ erg s^{-1} cm^{-2} arcsec^{-2} have also been overlaid, and the dashed white ellipse indicates the PSF in the final datacube with FWHM $\simeq 0.90'' \times 1.08''$ (X and Y-direction, respectively). Both images have been registered to the same world-coordinate system.

KCWI datacube using a 2D Gaussian filter with FWHM = 0.9″ (the seeing point spread function (PSF) measured from a bright star in the SSA22 field); (2) applying a 1D Gaussian spectral filter with FWHM = 500 km s^{-1} (a conservative lower limit on the observed Lyα line width estimated visually); (3) generating an S/N cube with the filtered datacube for thresholding.

We present the Lyα narrow-band image of LAB2 in the left panel of Figure 1. It is constructed by summing all the voxels of the continuum-subtracted filtered datacube with S/N $\geq$ 4 over 4949 – 5009 Å ($\sim$ –2000 – 1500 km s^{-1} at $z \sim 3.1$), which should enclose all possible Lyα emission. In the right panel, we present the *HST* WFC3-IR F160W rest-frame optical continuum image of LAB2[5] for comparison. The positions of previously identified sources are marked on each image as references. Thus far, multiple sources have been identified in LAB2: an LBG M14 (Steidel et al. 2000), an X-ray source (Basu-Zych & Scharf 2004; Lehmer et al. 2009a) with IR (LAB2-b, Webb et al. 2009) and submm (LAB2-ALMA, Ao et al. 2017) counterparts, and an IR source detected by *Spitzer* IRAC (LAB2-a, Webb et al. 2009). The detailed information for all the identified sources are presented in Table 2. The Lyα isophotes (contours with the same SB) with levels of $\mathrm{SB_{Ly\alpha}} = [150, 80, 40, 20, 10] \times 10^{-19}$ erg s^{-1} cm^{-2} arcsec^{-2} have also been overlaid onto each image.

In Figure 1, we see that the extended Lyα emission can be separated mainly in three distinct regions – the northeast (as indicated by a number '1'), the northwest (as indicated by a number '2'), and the south region. Among them, the south region has the largest extent. In this extended region there appears to be a high SB center (as indicated by a number '11'), yet neither M14 nor the X-ray source is close to this position – instead, they are located in the northeast outskirts where the Lyα SB is relatively low. In addition, the variation of the Lyα SB with respect to the maximum value is highly direction-dependent. Two regions exhibiting monotonically declining Lyα SB towards the northeast and southeast directions are evident, the former of which is more elongated.

3.2 Profiles of Lyα Emission & Blue-to-red Flux Ratio

The diverse Lyα profiles in three extended Lyα emitting regions as well as their outskirts are shown in Figure 2. The small northwest region exhibits a narrow double-peak profile with significant flux between the peaks. Both the northeast and the south region exhibit a similar pattern of an increase in the blue-to-red flux ratio ($F_{\rm blue}/F_{\rm red}$) towards the outer, lower SB regions. We illustrate this quantitatively in Figure 3.

To calculate the blue-to-red flux ratio of the spectrum of each pixel, we first identified the local minimum (trough) between two peaks of the continuum-subtracted, spatially and spectrally smoothed spectrum, and then integrated both blueward and redward until the flux density goes to zero. The blue-to-red flux ratio is simply the ratio of the integrated fluxes of the blue peak ($F_{\rm blue}$) and the red peak ($F_{\rm red}$). In the left panel of Figure 3, we show the spatial distribution of $F_{\rm blue}/F_{\rm red}$ of LAB2 with SB contours overlaid. It can be seen that $F_{\rm blue}/F_{\rm red}$ is lowest in the highest SB region, and increases outwards as the SB decreases. Regions with $F_{\rm blue}/F_{\rm red} > 1$ are evident in the outskirts at three different directions: north, southeast and southwest, which is potentially a signature of accreting gas (see e.g. Zheng & Miralda-Escudé 2002; Dijkstra et al. 2006b; Faucher-Giguère et al. 2010).

In the right panel of Figure 3, we show in a 2D density map

[5] The KCWI and *HST* images have been registered to the same world-coordinate system using cross-correlation.

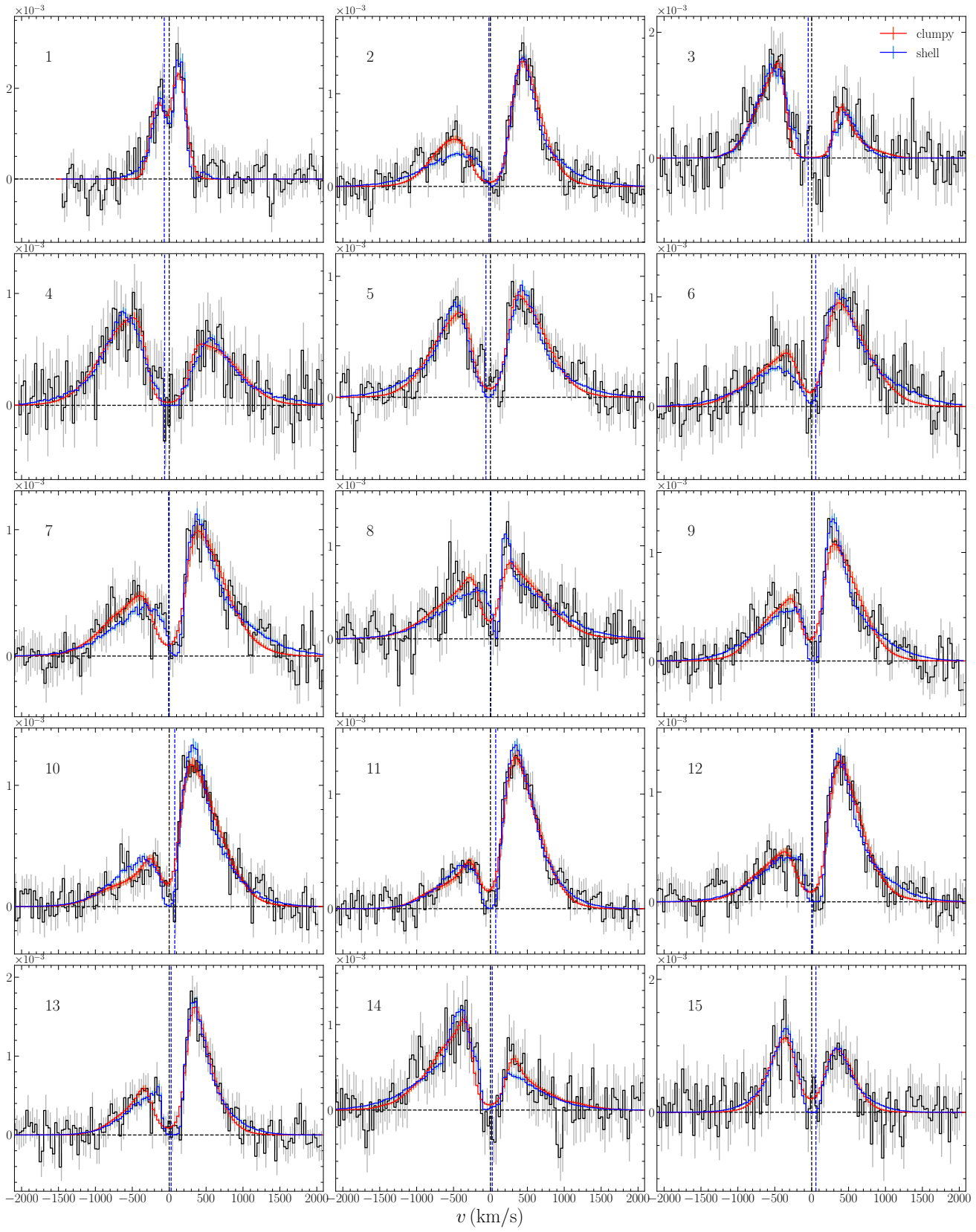

Figure 2. Fifteen representative continuum-subtracted, spatially-resolved and normalised Lyα profiles (black, with grey 1-σ error bars) from the high SB regions in LAB2. The spectrum number of each spectrum has been marked on the SB map in Figure 1. All the spectra have been smoothed by a 3 pixel × 3 pixel boxcar (0.9″) spatially and Gaussian smoothed (σ = 0.5 Å) in the wavelength dimension. As we will detail in §5.2.1, the multiphase, clumpy model best-fits (red, with orange 1-σ Poisson errors) and the shell model best-fits (blue, with cyan 1-σ Poisson errors) are both shown in each subpanel. The observed Lyα spectra have also been shifted by $-\Delta v_{\rm clumpy}$ to their local systemic redshifts (as determined by the best-fits), and the shell model best-fits are shifted correspondingly as well for direct comparison. For each subpanel, the x-axis is the velocity (in km s^{-1}) with respect to the local systemic redshift, and the y-axis is the normalised line flux. For visual reference, the horizontal and vertical black dashed lines in each subpanel indicate zero flux level and zero velocity with respect to the local systemic redshift, respectively. The vertical blue dashed lines indicate the initial guess for the systemic redshift (z = 3.09 for spectrum 1 and z = 3.098 for all other spectra).

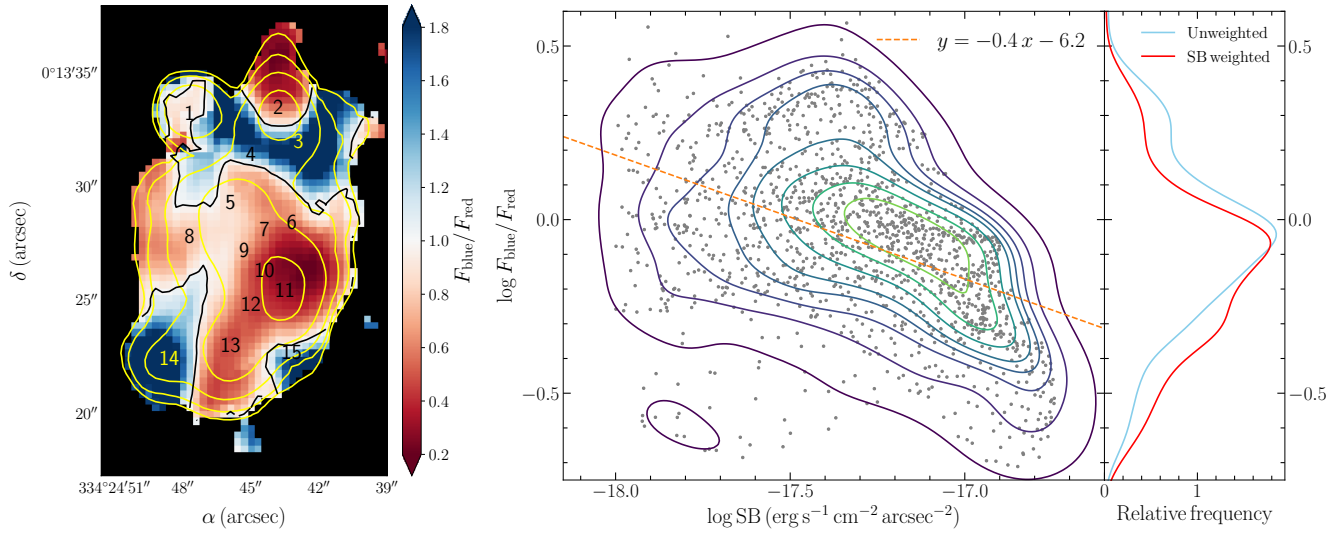

Figure 3. The spatial distribution of the blue-to-red flux ratio ($F_{\rm blue}/F_{\rm red}$) and its relation to SB. *Left:* The map of $F_{\rm blue}/F_{\rm red}$ of LAB2 with Lyα SB contours overlaid (same as in Figure 1 but in yellow color) and spectrum numbers marked (same as in Figure 1 but in yellow color for spectra 3 and 14 for clarity). The black contour indicates where $F_{\rm blue}/F_{\rm red} = 1$. It can be seen that $F_{\rm blue}/F_{\rm red}$ is the lowest in the highest SB region, and increases outwards as the SB decreases. *Right:* The 2D density map of $F_{\rm blue}/F_{\rm red}$ versus SB (on log scale) for all the individual pixels (as shown with grey points) with log SB > -18.0 (i.e. within the outermost yellow contour in the left panel). A simple power-law fit yields $F_{\rm blue}/F_{\rm red} \propto {\rm SB}^{-0.4}$, as shown in the orange dashed line. Note the anti-correlation between $F_{\rm blue}/F_{\rm red}$ and Lyα SB, which may be due to the decline of the projected line-of-sight outflow velocity and the increase of inflow velocity towards the blob outskirts. Also shown on the right are the unweighted (blue curve) and SB-weighted (red curve) frequency distributions of $F_{\rm blue}/F_{\rm red}$. Both distributions peak at $F_{\rm blue}/F_{\rm red} < 1$, where the SB-weighted one leans more towards lower $F_{\rm blue}/F_{\rm red}$.

how $F_{\rm blue}/F_{\rm red}$ varies with SB for all the individual pixels with log SB > -18.0 (i.e. within the outermost yellow contour in the left panel). We see that as SB increases, $F_{\rm blue}/F_{\rm red}$ (as shown with grey points) tends to decrease. A simple power-law fit yields $F_{\rm blue}/F_{\rm red} \propto {\rm SB}^{-0.4}$ (as shown in the orange dashed line). This trend may be due to a combination of: (1) the decline of the projected line-of-sight outflow velocity towards the outskirts of the halo (where the SB is low), assuming a central, roughly symmetric outflow exists (we will quantitatively test this hypothesis in §5.2.4); (2) the increase of inflow velocity at the blob outskirts. Such a transition from outflow to inflow-domination has been observed at ~ 50 kpc for a large sample of star-forming galaxies at $z \sim 2$ (Chen et al. 2020). We also show the unweighted and SB-weighted pixel frequency distributions of $F_{\rm blue}/F_{\rm red}$. Both distributions peak at $F_{\rm blue}/F_{\rm red} < 1$, where the SB-weighted one leans more towards lower $F_{\rm blue}/F_{\rm red}$. It suggests that our spatially-resolved (not SB-weighted) observations may be better at detecting blue-dominated Lyα profiles that would be otherwise missed in spatially-integrated (SB-weighted) observations.

The anti-correlation between the median $F_{\rm blue}/F_{\rm red}$ and SB observed here is similar to the trend observed by Erb et al. (2018), who studied the Lyα halo of a low-mass star-forming galaxy at $z = 2.3$ and found that the red peak dominates in the central, high SB region, whereas $F_{\rm blue}/F_{\rm red} \gtrsim 1$ in the outskirts of the halo. They also reported an anti-correlation between $F_{\rm blue}/F_{\rm red}$ and peak separation, which we do not observe in LAB2. Such a difference may reflect the intrinsic difference between Lyα halos illuminated by a single star-forming galaxy and by potentially multiple sources with various powering mechanisms (as in LAB2). We have also checked several other spectral properties, such as trough position, spectrum width and peak separation, but no significant trends have been found.

4 NON-DETECTION OF NEBULAR EMISSION LINES

In this section, we summarize the results of our MOSFIRE observations. We have searched through both slits for nebular emission lines and found no significant detection of [O III] or Hβ emission at any location (especially where the Lyα SB is the highest) on either slit within the region covered by LAB2. For the [O III]λ5008 line, we measured 2-σ flux upper limits of 2.8×10^{-18} and 2.5×10^{-18} erg s^{-1} cm^{-2} for Slit 1 and 2 respectively, using a window with spatial size of 3″ and spectral width of $\sigma = 75$ km s^{-1} assuming a systemic redshift of $z = 3.098$ (inferred from the following radiative transfer modelling in §5).

Although the non-detection of the nebular emission lines is puzzling, it is clear that the Lyα profiles near the high SB center are red-dominated and suggest the presence of outflows, which is most likely due to star formation or AGN-driven winds. It is therefore reasonable to hypothesize the existence of star-forming galaxies or AGNs hidden by dust extinction and/or contamination of a foreground source (see the right panel of Figure 1 for the location of a possible low-z interloper) near the Lyα SB peak. Our subsequent radiative transfer modelling analysis is also based on this assumed 'central powering + scattering' scenario[6].

5 RADIATIVE TRANSFER MODELLING USING THE MULTIPHASE CLUMPY MODEL

5.1 Methodology

To decode physical properties of the gas in LAB2 from the observational data, we used radiative transfer modelling to fit the spatially-resolved Lyα profiles. Similar to Li et al. (2021), we adopted a multiphase, clumpy model, which assumes cool, spherical H I clumps moving within a hot, ionized inter-clump medium (ICM) (Laursen et al. 2013; Gronke & Dijkstra 2016). The most crucial parameters of this model include: (1) the cloud covering factor ($f_{\rm cl}$), which is the mean number of clumps per line-of-sight from the center to

[6] One may speculate that the 'cold accretion' scenario can also produce red-dominated profiles if aided by IGM absorption preferentially on the blue side. However, such a scenario is likely to result in multiple (e.g. triple) peaks at $z \sim 3$, which we have not observed in LAB2 (Byrohl & Gronke 2020)

Table 3. Parameter values of the grids of models.

Model (1)	Parameter (2)	Definition (3)	Values (4)
Clumpy	$\log n_{\rm HI,\,ICM}$	ICM H I number density	(-7.5, -6.5, -5.5, -4.5, -4.0) log cm^{-3}
	$F_{\rm V}$	Volume filling factor	(0.1, 0.2, 0.4, 0.6)
	$\sigma_{\rm cl}$	Clump velocity dispersion	(0, 100, ..., 800) km s^{-1}
	$v_{\rm cl}$	Clump outflow velocity	(0, 100, ..., 800) km s^{-1}
	$\Delta v_{\rm clumpy}$	Velocity shift	[-200, 200] km s^{-1}
Shell	$v_{\rm exp}$	Shell expansion velocity	(0, 2, 5, 8, 10, 15, 20, 30, ..., 490) km s^{-1}
	$\log N_{\rm HI,shell}$	Shell H I column density	(16.0, 16.2, ..., 21.8) log cm^{-2}
	$\log T_{\rm shell}$	Shell (effective) temperature	(3.0, 3.4, ..., 5.8) log K
	$\sigma_{\rm i}$	Intrinsic spectrum width	[1, 800] km s^{-1} (continuous)
	$\Delta v_{\rm shell}$	Velocity shift	[-200, 200] km s^{-1} (continuous)

Notes. The parameter values of the model grids that we used for fitting the Lyα profiles. The columns are: (1) model type; (2) parameter name; (3) definition of the parameter; (4) parameter values on the grid. Note that negative values for $v_{\rm cl}$ and $v_{\rm exp}$ are also allowed in the fitting.

the boundary of the simulation sphere; (2) the residual[7] H I number density in the ICM ($n_{\rm HI,\,ICM}$), which determines the depth of the absorption trough; (3) the kinematics of the clumps, consisting of an isotropic Gaussian random motion (characterized by $\sigma_{\rm cl}$, the velocity dispersion of the clumps) and a symmetric radial outflow with a constant velocity $v_{\rm cl}$.

Note that Lyα radiative transfer in such a multiphase, clumpy medium exhibits two characteristic regimes defined by the values of $f_{\rm cl}$ (Gronke et al. 2016, 2017). If $f_{\rm cl}$ is much larger than a critical value $f_{\rm cl,crit}$ (which is a function of the H I column density and kinematics of the clumps, see Appendix B of Li et al. (2021) for a detailed derivation), the photons would escape as if the medium is homogeneous and the emergent spectra are similar to those predicted by the 'shell model' (Gronke et al. 2017). Otherwise, for a moderate number of clumps per line-of-sight, the photons preferentially travel in the hot ionized ICM and escape close to the Lyα line center.

We constructed a four-dimensional hypercubic grid of models by varying the aforementioned four crucial physical parameters: $[\log n_{\rm HI,\,ICM}, F_{\rm V}, \sigma_{\rm cl}, v_{\rm cl}]$[8]. The prior ranges of the parameters are summarized in Table 3. We fixed the subdominant parameters, such as the clump temperature $T_{\rm cl}$ to 10^4 K, the ICM temperature $T_{\rm ICM}$ to 10^6 K, and the clump column density to 10^{17} cm^{-2} (McCourt et al. 2018) in order to reduce the dimensionality of the parameter space. We varied an additional parameter, $\Delta v_{\rm clumpy}$, continuously in post-processing[9]. This $\Delta v_{\rm clumpy}$ parameter represents the best-fit systemic redshift of the Lyα source function relative to z = 3.098 (the initial guess for the systemic redshift – it is where the trough of most Lyα spectra is located)[10]. Furthermore, we considered *inflow* velocities (i.e. $v_{\rm cl} < 0$) by mirroring the model spectra with respect to the line center.

Such a configuration amounts to 1620 models in total. Each model is calculated via radiative transfer using 10000 Lyα photon packages generated from a Gaussian intrinsic spectrum $N(0, \sigma^2_{\rm i,cl})$, where $\sigma_{\rm i,cl}$ = 12.85 km s^{-1} is the canonical thermal velocity dispersion of $T = 10^4$ K gas. To properly explore the multimodal posterior of the parameters, we used a python nested sampling package `dynesty` (Skilling 2004, 2006; Speagle 2020) for our fitting pipeline.

[7] Here we have assumed that the hydrogen in the hot ICM is highly ionized and only a very small fraction exists in the form of H I (i.e. $x_{\rm HI,\,ICM} \ll 1$).
[8] For convenience we varied $F_{\rm V}$ rather than $f_{\rm cl}$ when generating clumps. These two parameters are proportionally related via the relation $f_{\rm cl} = 3r_{\rm gal}/4r_{\rm cl}\,F_{\rm V}$, where $r_{\rm gal}$ = 5 kpc is the radius of the simulation sphere and $r_{\rm cl}$ = 50 pc is the clump radius (hence $f_{\rm cl} = 75\,F_{\rm V}$ in our case).
[9] Different from Li et al. (2021), we set the ICM as static (i.e. $v_{\rm ICM} = 0$), as we found that $v_{\rm ICM}$ is degenerate with $\Delta v_{\rm clumpy}$ (i.e. forcing $v_{\rm ICM}$ to be 0 simply yields $\Delta v_{\rm clumpy} \rightarrow \Delta v_{\rm clumpy} - v_{\rm ICM}$).
[10] Note that the northeast Lyα emitting region is located at a lower redshift, z = 3.09, which we adopted as the initial guess for spectrum 1.

5.2 Results

5.2.1 *Fits & Derived Parameters*

We selected fifteen representative Lyα spectra from the high SB regions in LAB2 for further model fitting. The positions of these spectra are shown in Figure 1, and the profiles are shown in Figure 2. All spectra were extracted at the center of a 3 pixel × 3 pixel boxcar from the spatially and spectrally smoothed KCWI datacube.

In addition to using the multiphase, clumpy models to fit the Lyα spectra, we also adopted the widely used 'shell model' (e.g. Ahn et al. 2003; Verhamme et al. 2006; Dijkstra et al. 2006b). A similar three-dimensional cubic grid of shell models was constructed by varying three parameters: the shell expansion velocity $v_{\rm exp}$, the shell H I column density $\log N_{\rm HI,\,shell}$, and the effective temperature of H I in the shell, $\log T_{\rm shell}$. Two more parameters, namely the intrinsic line width $\sigma_{\rm i}$ and the velocity shift with respect to the initial guess for the systemic redshift (z = 3.09 for spectrum 1 and z = 3.098 for all other spectra), $\Delta v_{\rm shell}$, are varied continuously in post-processing[11].

During the fitting procedure, each model spectrum is calculated via linear flux interpolation on the model grid and is convolved with the KCWI line-spread function (LSF, a Gaussian with σ = 65 km s^{-1}) before being compared to the observed Lyα profiles. To better reproduce the profiles dominated by a blue peak (e.g. spectra 3, 4, 14 and 15), we have also incorporated model spectra with negative $v_{\rm cl}$ or $v_{\rm exp}$ that have been 'mirrored' in the velocity space from their positive $v_{\rm cl}/v_{\rm exp}$ counterparts into our calculation. The best-fit model spectra are also shown in Figure 2.

In Figure 2, one can see that, in most cases, both the multiphase, clumpy model fits and shell model fits match the observed Lyα profiles reasonably well. The values of the fitted parameters are presented in Table 4, and the derived joint and marginal posterior probability distributions are presented in Appendix A. One prominent difference between the fits of two different models is that many multiphase, clumpy model fits have residual flux density at the Lyα line center, whereas the shell model fits almost always have zero flux density at the minimum. This is because $[f_{\rm cl}, n_{\rm HI,\,ICM}]$ and $N_{\rm HI,\,shell}$ are responsible for setting the peak separation in the respective model. In the shell model, the required $N_{\rm HI,\,shell}$ by the data is $\gtrsim 10^{19}$ cm^{-2}, which already corresponds to a very high maximum optical depth that yields saturated absorption. Whereas in the multiphase, clumpy model, the required $f_{\rm cl}$ and $n_{\rm HI,\,ICM}$ by the data only correspond to a moderate optical depth that still allows Lyα photons to escape at line center.

Motivated by the fact that certain parameters from both models should control similar Lyα spectral properties, we further attempted to find the link between the two models by correlating parameter pairs. We have observed two significant ($\gtrsim 5\sigma$) positive correlations between: (1) $\sigma_{\rm cl}$ and $\sigma_{\rm i}$; (2) $v_{\rm cl}$ and $v_{\rm exp}$. We have also performed linear regressions to these correlations and estimated the uncertainties in the coefficients (slope m and intercept b) by perturbing the data points with asymmetric Gaussian noise with amplitude proportional to the error bars. The results are shown in Figure 4.

The existence of these two significant correlations can be easily understood since the parameter pairs control the same spectral properties, namely the spectrum width and the red-to-blue flux ratio. Interestingly, we see that $\sigma_{\rm cl} \leq \sigma_{\rm i}$ and $|v_{\rm cl}| \geq |v_{\rm exp}|$ are almost always true. **These results naturally alleviated the tension between the fitted shell model parameters and the observational constraints** reported in e.g. Orlitová et al. (2018), namely: (1) the

[11] The detailed configuration of the shell model is presented in Gronke et al. (2015), and an example of fitting Lyα spectra with a grid of shell models is presented, for instance, in Gronke (2017).

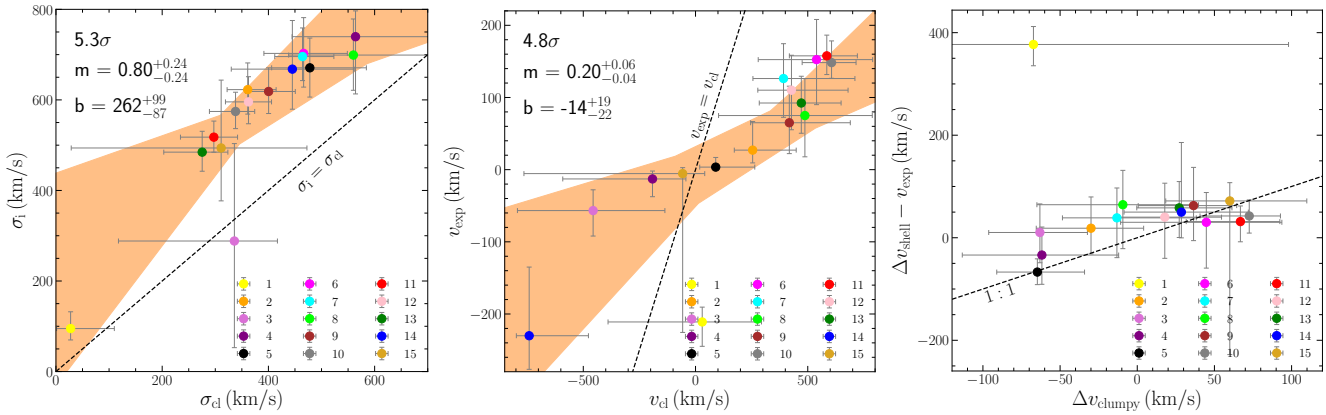

Figure 4. Correlations between the multiphase, clumpy model parameters and the shell model parameters. Two significant ($\gtrsim 5\sigma$) positive correlations exist between: (1) v_{cl} and v_{exp}; (2) σ_{cl} and σ_i. The Δv_{clumpy} v.s. $\Delta v_{shell} - v_{exp}$ correlation is insignificant, but the data points (excluding spectra 1 and 3) are broadly consistent with a 1-to-1 relation within 2σ uncertainties. The color-coded points represent different Lyα spectra (see Figure 1 and 2). The 2-σ uncertainties of the data points are indicated by grey error bars. The level of significance of each correlation and the linear best-fit coefficients (slope m and intercept b, with 1-σ uncertainties) are shown at the upper left corner in each panel. The orange shaded region represent the range of twenty best-fits of the data points perturbed by their uncertainties.

Table 4. Fitted parameters and derived quantities of the multiphase, clumpy model and the shell model.

			Clumpy Model Parameters					Derived Parameters		Shell Model Parameters				
No.	RA (J2000)	Dec (J2000)	$\log n_{HI,ICM}$ (cm^{-3})	F_V	σ_{cl} (km s^{-1})	v_{cl} (km s^{-1})	Δv_{clumpy} (km s^{-1})	$f_{cl}/f_{cl,crit}$	$\log \tau_{0,ICM}$	v_{exp} (km s^{-1})	$\log N_{HI,shell}$ (cm^{-2})	$\log T_{shell}$ (K)	σ_i (km s^{-1})	Δv_{shell} (km s^{-1})
(1)	(2)	(3)	(4)	(5)	(6)	(7)	(8)	(9)	(10)	(11)	(12)	(13)	(14)	(15)
1	22:17:39.179	+00:13:33.17	$-7.21^{+0.39}_{-0.25}$	$0.42^{+0.18}_{-0.30}$	27^{+82}_{-26}	29^{+263}_{-419}	-67^{+165}_{-94}	$27.0^{+17.1}_{-21.3}$	$0.7^{+0.4}_{-0.3}$	-211^{+20}_{-33}	$19.5^{+0.1}_{-0.2}$	$4.4^{+0.9}_{-1.2}$	94^{+37}_{-25}	165^{+28}_{-24}
2	22:17:38.919	+00:13:33.47	$-5.01^{+0.78}_{-0.58}$	$0.46^{+0.13}_{-0.18}$	361^{+53}_{-38}	254^{+194}_{-81}	-29^{+34}_{-35}	$5.7^{+2.3}_{-2.5}$	$3.0^{+0.8}_{-0.6}$	27^{+39}_{-17}	$20.5^{+0.5}_{-0.5}$	$3.4^{+1.1}_{-0.4}$	622^{+58}_{-54}	45^{+46}_{-46}
3	22:17:38.859	+00:13:31.97	$-4.25^{+0.24}_{-0.58}$	$0.25^{+0.28}_{-0.11}$	335^{+81}_{-218}	-456^{+319}_{-337}	-63^{+30}_{-33}	$3.7^{+7.3}_{-1.7}$	$3.7^{+0.2}_{-0.6}$	-56^{+28}_{-35}	$20.4^{+0.3}_{-0.3}$	$5.5^{+0.2}_{-0.6}$	288^{+215}_{-235}	-46^{+47}_{-47}
4	22:17:38.999	+00:13:31.37	$-4.82^{+0.74}_{-0.95}$	$0.42^{+0.16}_{-0.19}$	564^{+156}_{-119}	-191^{+148}_{-399}	-61^{+49}_{-51}	$3.4^{+2.4}_{-1.9}$	$3.1^{+0.7}_{-0.9}$	-12^{+10}_{-24}	$20.9^{+0.7}_{-0.4}$	$4.8^{+0.7}_{-1.3}$	739^{+57}_{-126}	-46^{+53}_{-51}
5	22:17:39.059	+00:13:29.27	$-5.56^{+0.58}_{-0.47}$	$0.33^{+0.15}_{-0.14}$	477^{+106}_{-71}	89^{+173}_{-71}	-64^{+30}_{-26}	$3.1^{+2.0}_{-1.6}$	$2.4^{+0.6}_{-0.5}$	3^{+13}_{-3}	$20.8^{+0.5}_{-0.5}$	$4.4^{+0.9}_{-0.9}$	670^{+65}_{-64}	-63^{+22}_{-24}
6	22:17:38.879	+00:13:28.37	$-6.00^{+0.64}_{-0.50}$	$0.36^{+0.14}_{-0.13}$	466^{+82}_{-74}	539^{+249}_{-259}	44^{+48}_{-55}	$3.4^{+1.8}_{-1.3}$	$2.0^{+0.6}_{-0.5}$	152^{+55}_{-62}	$19.4^{+0.4}_{-0.3}$	$4.0^{+1.0}_{-0.9}$	702^{+79}_{-74}	182^{+16}_{-63}
7	22:17:38.959	+00:13:28.07	$-5.78^{+0.64}_{-0.59}$	$0.39^{+0.11}_{-0.13}$	464^{+59}_{-52}	391^{+318}_{-136}	-13^{+51}_{-35}	$3.7^{+1.5}_{-1.4}$	$2.2^{+0.6}_{-0.6}$	126^{+48}_{-53}	$19.3^{+0.3}_{-0.3}$	$4.4^{+0.5}_{-1.3}$	695^{+63}_{-53}	165^{+32}_{-56}
8	22:17:39.179	+00:13:27.77	$-6.21^{+0.75}_{-0.35}$	$0.21^{+0.13}_{-0.08}$	559^{+148}_{-121}	487^{+300}_{-384}	-9^{+48}_{-55}	$1.7^{+1.3}_{-0.8}$	$1.7^{+0.7}_{-0.4}$	74^{+51}_{-57}	$18.6^{+0.8}_{-2.1}$	$4.0^{+0.8}_{-1.0}$	699^{+79}_{-77}	139^{+43}_{-63}
9	22:17:39.019	+00:13:27.17	$-6.35^{+0.36}_{-0.19}$	$0.25^{+0.13}_{-0.07}$	400^{+50}_{-43}	417^{+271}_{-172}	36^{+27}_{-35}	$2.8^{+1.7}_{-0.8}$	$1.6^{+0.4}_{-0.2}$	64^{+50}_{-42}	$19.4^{+0.6}_{-0.5}$	$4.2^{+0.6}_{-1.1}$	618^{+52}_{-48}	127^{+54}_{-53}
10	22:17:38.959	+00:13:26.27	$-6.41^{+0.31}_{-0.09}$	$0.46^{+0.09}_{-0.07}$	338^{+36}_{-49}	605^{+109}_{-130}	72^{+20}_{-31}	$6.2^{+1.7}_{-1.2}$	$1.5^{+0.3}_{-0.1}$	148^{+30}_{-21}	$19.3^{+0.1}_{-0.1}$	$4.6^{+0.3}_{-1.5}$	574^{+42}_{-37}	190^{+8}_{-25}
11	22:17:38.899	+00:13:25.37	$-6.18^{+0.34}_{-0.28}$	$0.42^{+0.09}_{-0.07}$	297^{+44}_{-62}	584^{+136}_{-166}	66^{+25}_{-35}	$6.3^{+2.9}_{-1.3}$	$1.8^{+0.3}_{-0.3}$	157^{+28}_{-25}	$19.4^{+0.1}_{-0.1}$	$4.7^{+0.3}_{-1.6}$	517^{+35}_{-33}	189^{+10}_{-29}
12	22:17:38.999	+00:13:24.77	$-5.78^{+0.46}_{-0.52}$	$0.35^{+0.13}_{-0.11}$	362^{+43}_{-43}	427^{+252}_{-149}	17^{+36}_{-32}	$4.4^{+1.9}_{-1.4}$	$2.2^{+0.5}_{-0.5}$	110^{+48}_{-54}	$19.5^{+0.4}_{-0.3}$	$4.3^{+0.7}_{-1.3}$	595^{+55}_{-48}	150^{+45}_{-58}
13	22:17:39.059	+00:13:22.97	$-5.67^{+0.31}_{-0.48}$	$0.24^{+0.11}_{-0.07}$	275^{+48}_{-72}	471^{+177}_{-187}	27^{+34}_{-27}	$3.9^{+2.2}_{-1.2}$	$2.3^{+0.3}_{-0.5}$	92^{+37}_{-41}	$19.4^{+0.4}_{-0.3}$	$5.0^{+0.2}_{-1.8}$	484^{+46}_{-42}	150^{+35}_{-39}
14	22:17:39.239	+00:13:22.37	$-5.71^{+0.45}_{-0.46}$	$0.30^{+0.18}_{-0.13}$	445^{+116}_{-115}	-740^{+263}_{-57}	28^{+43}_{-37}	$3.1^{+2.1}_{-1.5}$	$2.3^{+0.4}_{-0.5}$	-230^{+95}_{-46}	$18.7^{+0.8}_{-2.5}$	$5.0^{+0.5}_{-1.7}$	667^{+107}_{-88}	-180^{+96}_{-18}
15	22:17:38.879	+00:13:22.67	$-6.19^{+0.55}_{-0.82}$	$0.27^{+0.30}_{-0.16}$	311^{+161}_{-282}	-57^{+98}_{-707}	59^{+49}_{-41}	$4.1^{+21.3}_{-2.9}$	$1.8^{+0.5}_{-0.8}$	-5^{+8}_{-220}	$20.4^{+0.6}_{-2.7}$	$4.6^{+0.5}_{-1.2}$	493^{+149}_{-116}	66^{+34}_{-203}

Notes. Fitted parameters (averages and 2.5% – 97.5% quantiles, i.e. 2-σ confidence intervals) of the multiphase clumpy model and shell model, and derived quantities. The columns are: (1) the spectrum number (as marked in Figure 2); (2) the right ascension of the center of the extracted region; (3) the declination of the center of the extracted region; (4) the H I number density in the ICM; (5) the cloud volume filling factor; (6) the velocity dispersion of the clumps; (7) the radial outflow velocity of the clumps; (8) the velocity shift relative to the initial guess for the systemic redshift ($z = 3.09$ for spectrum 1 and $z = 3.098$ for all other spectra; a negative/positive value means that the best-fit model spectrum has been blue/redshifted to match the data); (9) the clump covering fraction (defined as the number of clumps per line-of-sight) normalised by the critical clump covering fraction. In our case $f_{cl} = 75\,F_V$. The critical clump covering fraction, $f_{cl,crit}$, determines different physical regimes and is calculated via Eq. (B3) in Li et al. (2021); (10) the optical depth at the Lyα line center of the H I in the ICM; (11) the expansion velocity of the shell; (12) the H I column density of the shell; (13) the H I temperature of the shell; (14) the required intrinsic line width; (15) the velocity shift relative to the initial guess for the systemic redshift.

required σ_i are on average three times broader than the observed non-resonant Balmer lines; (2) the derived v_{exp} are smaller than the outflow velocities determined from UV absorption lines. This suggests that the photon scattering between randomly moving clumps may be an efficient way of broadening Lyα profiles and circumventing overlarge σ_i (see also Hashimoto et al. 2015), and that v_{cl} in the clumpy medium is less efficient at increasing the spectrum asymmetry than v_{exp}. Such distinctions reflect the intrinsic differences between two models: in the shell model, all the photons have to traverse the shell and thus are shaped by the same shell outflow/inflow

velocity; whereas in the multiphase, clumpy model, the photons can randomly walk between the clumps or even diffuse outwards with their frequencies unaffected[12] (Neufeld 1991; Gronke & Dijkstra 2016). This means that the effective outflow velocity 'experienced' by the photons in the multiphase, clumpy model is smaller than that in the shell model, which needs to be compensated by a larger $v_{\rm cl}$. Furthermore, as scattering orthogonally off the flowing clumps may yield additional broadening to the spectra (Li et al. 2021), the $\sigma_{\rm cl}$ values required to achieve the large observed widths of Lyα profiles are lower.

By the same token, correlations between (1) $n_{\rm HI,\,ICM}$ (and $F_{\rm V}$[13]) and $N_{\rm HI,\,shell}$; (2) $\Delta v_{\rm clumpy}$ and $\Delta v_{\rm shell} - v_{\rm exp}$ may exist, as they control the peak separation and trough position[14], respectively. However, we found that the former correlation is insignificant, as the best-fits from two models prefer different peak separations in many cases (see e.g. spectra 7, 8, 10 and 13). The latter correlation is also insignificant ($\lesssim 2\sigma$) with two apparent outliers – for spectrum 1, the multiphase, clumpy model prefers outflow, whereas the shell model prefers inflow; for spectrum 3, the absorption for both best-fits are saturated so that extended troughs are produced. The other 13 data points are broadly consistent with a 1-to-1 relation within 2σ uncertainties. **Such a correspondence between $\Delta v_{\rm clumpy}$ and $\Delta v_{\rm shell} - v_{\rm exp}$ may resolve an additional inconsistency** reported in Orlitová et al. (2018), i.e. the best-fit systemic redshifts ($\Delta v_{\rm shell}$) from the shell model are larger by 10 – 250 km s^{-1} than those determined from optical emission lines. Further observations of non-resonant lines that are available for other objects are necessary for a decisive conclusion.

We have not found any straightforward analytic mapping functions that can directly convert the best-fit parameters from one model to the other. In our future work, we will explore whether such analytic mapping functions exist between certain parameters first in the $f_{\rm cl} \gg f_{\rm cl,crit}$ regime, and then in the regime that we have explored in this work, i.e. $f_{\rm cl}$ is higher than $f_{\rm cl,crit}$ but mostly within one order of magnitude, where only qualitative trends between parameter pairs have been observed.

Although the shell model fits have comparable likelihoods to the multiphase, clumpy model fits, they are less likely to be informative of the actual physical conditions in the circumgalactic medium (CGM), because (1) the shell model only has a single phase of H I with low-to-medium effective temperature ($T_{\rm shell} \sim 10^{4-5}$K); (2) the aforementioned $v_{\rm exp}, \sigma_{\rm i}$ and $\Delta v_{\rm shell}$ values that are inconsistent with the observational constraints (e.g. Orlitová et al. 2018). Whereas the multiphase, clumpy model is not only likely a more realistic description of the CGM (Tumlinson et al. 2017), but it also yields more reasonable physical parameters (as we will elaborate below). Therefore, we will focus on the multiphase, clumpy model in the rest of this paper.

5.2.2 *Interpretation of Fitted Parameters*

In this section, we discuss how realistic the fitted parameters of the multiphase, clumpy model are compared to other studies.

(i) *Covering fraction of the cool clumps*: The derived volume filling factors ($F_{\rm V}$) range from ~ 0.2 – 0.5, which convert to covering factors ($f_{\rm cl}$) of ~ 15 – 40. Such high covering factors effectively correspond to covering *fractions* of unity[15] (Laursen et al. 2013). This result is consistent with the recent findings in Wisotzki et al. (2018), where they observed low SB Lyα emission surrounding high-z faint galaxies with MUSE and claimed that the H I covering fractions around galaxies should be sufficiently close to unity at $z > 3$, assuming the spatial distribution of circumgalactic H I is similar to the Lyα-emitting gas. Additionally, high H I covering fractions around galaxies have also been observed at lower redshifts ($z < 2$, see e.g. Chen et al. 2001; Prochaska et al. 2011; Rudie et al. 2012; Tumlinson et al. 2013), suggesting that large H I covering fractions should be universally present across different cosmic epochs.

(ii) *Velocity of the cool clumps*: The derived clump velocity dispersions ($\sigma_{\rm cl}$) range from $\sim$ 300 – 600 km s^{-1}, which correspond to a dynamical halo mass of $\rm M_{dyn} \sim 10^{13} M_\odot$, consistent with the predicted halo masses from the Millennium simulations (see Eq. 3 in Li et al. 2021 and discussions therein). The clump outflow velocities ($v_{\rm cl}$) range from $\sim$ 100 – 500 km s^{-1}, which yield considerable cloud lifetimes (or even cloud growth) in the hot ICM (Gronke & Oh 2018; Li et al. 2020, 2021). Future observations may provide additional constraints on the relative velocities between the cool clumps and the ICM derived from simplistic configurations in this work.

In terms of the survival of cool clumps, it is also helpful to consider the thermal sound speed of the hot ICM, $c_{s,\,\rm ICM} \sim \sqrt{k_B T_{\rm ICM}/m_{\rm p}} \sim 100\,{\rm km\,s^{-1}}$. Therefore, the Mach numbers of the cool clumps $\mathcal{M}_{\rm cl} \equiv v_{\rm cl}/c_{s,\,\rm ICM}$ or $\sigma_{\rm cl}/c_{s,\,\rm ICM} \sim 1-5$, which are transonic or mildly supersonic. These Mach numbers are realistic for circumgalactic gas, and may slightly affect the dynamics of the cool clumps in the hot medium (see e.g. Scannapieco & Brüggen 2015; Sparre et al. 2020).

(iii) *Energy contribution from the inflowing gas*: We have observed signatures of gas inflow at the blob outskirts (see the blue-peak dominated spectra 3, 4, 14 and 15 and the inferred negative 'outflow' velocities), and it is possible to estimate the associated cooling luminosity. The mass flow rate of the inflowing H I gas is given by:

$$\dot{M_{\rm HI}} = 4\pi R_{\rm h}^2 \rho_{\rm HI} \frac{dr}{dt} = 4\pi R_{\rm h}^2 \rho_{\rm HI} v_{\rm inflow} \tag{1}$$

where $R_{\rm h}$ is the halo radius and $v_{\rm inflow}$ is the gas inflow velocity. The H I mass density, $\rho_{\rm HI}$, is given by:

$$\rho_{\rm HI} = \frac{M_{\rm HI}}{V_{\rm h}} = \frac{n_{\rm HI,clump} m_{\rm H} r_{\rm cl}^3 N_{\rm clumps}}{R_{\rm h}^3} \tag{2}$$

where $n_{\rm HI,clump}$ is the clump H I number density, $m_{\rm H}$ is the mass of a hydrogen atom, and $r_{\rm cl}$ is the clump radius. The total number of clumps in the halo, $N_{\rm clumps}$, is related to the volume filling factor:

$$F_{\rm V} = \frac{N_{\rm clumps} r_{\rm cl}^3}{R_{\rm h}^3} \tag{3}$$

With all these relations, the cooling luminosity generated from the released gravitational energy by gas infalling is:

$$L_{\rm cool} = \frac{G M_{\rm h} \dot{M_{\rm HI}}}{R_{\rm h}} = 4\pi G M_{\rm h} F_{\rm V} f N_{\rm HI,clump} m_{\rm H} v_{\rm inflow} \tag{4}$$

$$= 1.4 \times 10^{42} F_{\rm V} \left(\frac{M_{\rm h}}{10^{13} M_\odot}\right) \left(\frac{v_{\rm inflow}}{100\,{\rm km\,s^{-1}}}\right) {\rm erg\,s^{-1}} \tag{5}$$

[12] Note that we focused on the $f_{\rm cl}/f_{\rm cl,crit} \simeq 1-10$ regime in this work.

[13] Both $n_{\rm HI,\,ICM}$ and $F_{\rm V}$ (or $f_{\rm cl}$) contribute to the effective column density in the multiphase, clumpy model (see Eq. (1) in Gronke & Dijkstra 2016).

[14] Note that we have set $v_{\rm ICM}$ = 0 in this work; otherwise a correlation between $\Delta v_{\rm clumpy} - v_{\rm ICM}$ and $\Delta v_{\rm shell} - v_{\rm exp}$ (where the optical depth is at the maximum) is expected in a moving ICM.

[15] This is true especially in the central region; in the outskirts the covering fraction may decrease even for a homogeneous clump distribution (as assumed in this work). Technically, the effective covering factor to an external observer is $\tilde{f_{\rm cl}} = f_{\rm cl} \frac{2\sqrt{R^2-b^2}}{R}$, which corresponds to an (area) covering fraction of $f_{\rm A}(b) = 1 - \exp(\tilde{f_{\rm cl}})$, i.e. one minus the Possion probability of photons intersecting with zero clumps. Here R is the radius of the studied region, and b is the projected distance from the center of the region relative to the line-of-sight.

Note that we have fixed $N_{\rm HI,clump} = 10^{17}\,{\rm cm}^{-2}$, and f is the radius ratio of the halo and the clumps (100 in our radiative transfer calculations). Taking $F_{\rm V} \sim 0.5$, $M_{\rm h} \sim 10^{13} M_\odot$ and $v_{\rm inflow} \sim 400\,{\rm km\,s}^{-1}$(the median of the derived inflow velocities[16]), we get $L_{\rm cool} \sim 3 \times 10^{42}\,{\rm erg\,s}^{-1}$. This value is still more than one order of magnitude lower than the observed Lyα luminosity of LAB2, even if all the cooling luminosity is emitted in Lyα. Therefore, we conclude that the infalling of cool gas (cold accretion) plays a minor role in powering LAB2. This conclusion is consistent with the recent result of Ao et al. (2020), where they also found for a $z \sim 2.3$ LAB that cool gas infalling helps produce blue-peak dominated Lyα profiles, but is a subdominant powering mechanism compared to the photo-ionization process by embedded star-forming galaxies and/or AGNs.

(iv) *Residual H I density in the ICM*: The derived H I number densities correspond to column densities of $n_{\rm HI,ICM} r_{\rm gal} \sim 10^{15} - 10^{18}\,{\rm cm}^{-2}$ (recall that $r_{\rm gal} = 5\,{\rm kpc}$ is the radius of the simulation sphere) and Lyα optical depths at line center of $\tau_{0,\rm ICM} \sim 10 - 10^3$. Such column densities are high enough to contribute to the broadening of Lyα spectra and produce (unsaturated) absorption at the line center. Taking the LAB2 halo radius as $R_{\rm h} \sim 50$ kpc, the derived $n_{\rm HI,ICM}$ values correspond to actual residual H I number densities of $\sim 10^{-8} - 10^{-5}\,{\rm cm}^{-3}$. These values are moderately higher than the expected values assuming collisional ionization equilibrium, i.e. hydrogen number density $n_{\rm H,ICM} \sim 10^{-3} - 10^{-2}\,{\rm cm}^{-3}$ and H I fraction $x_{\rm HI,ICM} \sim 10^{-6}$ at $T_{\rm ICM} = 10^6$K (Dopita & Sutherland 2003), but the difference is not significant especially considering that the highest $n_{\rm HI,ICM}$ values (e.g. spectra 2 – 5) appear close to the X-ray/submm continuum sources, which may be due to galactic feedback (see e.g. §2.2 of McQuinn 2016).

5.2.3 *Fitting Spectra at Different Spatial Positions Simultaneously*

In this section, we attempt to fit multiple spatially-resolved Lyα profiles with multiphase, clumpy models in a more self-consistent way. We demonstrate that we can fit Lyα spectra at different distances from a high SB center (i.e. at different impact parameters) simultaneously in one fitting run[17].

As illustrated in Figure 5, we chose spectra from three equally-spaced regions along a line (in projection) with respect to the high SB center (spectra 9, 10 and 11) to perform our fit. For each model calculated in the fitting procedure, the Lyα photon packages (10000 in total) are separated into three different bins, according to the impact parameter[18] of their last-scattering locations: $0.05 < b/b_{\rm max} \leq 0.35$, $0.35 < b/b_{\rm max} \leq 0.65$ and $0.65 < b/b_{\rm max} \leq 0.95$, where $b_{\rm max}$ is the largest impact parameter of all the scattered Lyα photons. In this way, the representative photons included in each bin are numerous enough to construct a meaningful model spectrum. At every likelihood evaluation call, each observed Lyα spectrum is compared to the corresponding 'binned' model spectrum, and the likelihood is simply the sum of the likelihoods of three binned models.

The fitting results are shown in Figure 5. We found that the likelihoods of the binned fits are comparable to those of the individual fits (which were obtained by fitting spectra at each location independently). Moreover, the derived $v_{\rm cl}$ of this 'combined fit' is fully consistent with the value of the individual fit of spectrum 11. One notable discrepancy is that the outermost binned model ($0.65 < b/b_{\rm max} \leq 0.95$) failed to fully reproduce the Lyα flux density minimum near the systemic velocity of spectrum 9, which may be due to the assumption that $n_{\rm HI,ICM}$ is constant over the whole simulated region, whereas in reality the residual H I density in the ICM may vary spatially or extend beyond the multiphase medium. It is therefore possible to remedy this mismatch by considering models with radially-varying $n_{\rm HI,ICM}$. Nevertheless, we have demonstrated the possibility of fitting spectra with different impact parameters simultaneously in a self-consistent manner. Further applications and extensions to the model are left to future work.

5.2.4 $v_{\rm cl}$ *v.s. b: A Simple Projection?*

As presented in Table 4, the inferred outflow velocities of the cool clumps, $v_{\rm cl}$, vary significantly at different positions. Here we test whether this variation can be consistent with being a projection effect, i.e. the derived $v_{\rm cl}$ values from the multiphase, clumpy models are simply the projected line-of-sight components of an isotropic outflow velocity.

The line-of-sight component of an isotropic outflow velocity is given by (as illustrated in the left panel of Figure 6):

$$\begin{aligned} v_{\rm LOS} &= v_{\rm iso}\cos\theta \\ &= v_{\rm iso}\sqrt{1-(b/b_{\rm max})^2} \end{aligned} \quad (6)$$

where $v_{\rm LOS}$ is the observed line-of-sight outflow velocity, $v_{\rm iso}$ is the isotropic outflow velocity, θ is the angle between the line-of-sight and the isotropic outflow velocity, b is the impact parameter of the observed location, and $b_{\rm max}$ is the maximum impact parameter of the observed region (or the radius if the region is spherically symmetric). We further examined Eq. (6) by plotting the $v_{\rm cl}$ values derived from individual fits[19] along with the range of fitted $v_{\rm cl}$ v.s. b curves in the right panel of Figure 6. A reference $v_{\rm cl}$ v.s. b curve from the combined fit of spectra 9, 10 and 11 is also plotted for comparison, which is generated by setting $v_{\rm iso} = 604^{+36}_{-46}\,{\rm km\,s}^{-1}$ (the $v_{\rm cl}$ of the combined fit of spectra 9, 10 and 11) and $b_{\rm max} = 33\,{\rm kpc}$ (calculated by mapping the geometric distances in the model to the actual physical distances[20]) in Eq. (6).

As can be seen in Figure 6, the reference $v_{\rm cl}$ v.s. b curve from the combined fit (blue solid and dashed lines) is fairly consistent with the $v_{\rm cl}$ values derived from individual fits (as well as the fitted $v_{\rm iso}$ and $b_{\rm max}$ values) within 1-σ uncertainties, suggesting the variations in $v_{\rm cl}$ may be simply the projection of a radial outflow along the line-of-sight. Therefore, we conclude that the observed variation in $v_{\rm cl}$ with respect to b can be reasonably accounted for by a simple line-of-sight projection effect. This would also naturally explain the observed increase in $F_{\rm blue}/F_{\rm red}$ ratio towards the blob outskirts, as $F_{\rm blue}/F_{\rm red}$ is inversely correlated with $v_{\rm cl}$ (see §3.2), although the blue-dominated spectra at the very largest distances require inflows.

6 PREVIOUS STUDIES OF LAB2

Here we summarize the results of previous studies of LAB2 and compare with the present work. We classify different studies according to the wavelengths of their observations:

[16] Note that the values of inferred inflow velocities (spectra 3, 4, 14 and 15) all have considerable uncertainties.

[17] We have also attempted to fit spectra at different spatial positions assuming an identified continuum source (e.g. M14 or the X-ray source) as the central Lyα emitting source, but these attempts turned out to be unsuccessful. This is because in an outflow model the inner photons tend to be more red-dominated than the outer photons, which is opposite to the observed trend away from any continuum source (cf. §3.2)

[18] Here we define impact parameter b as the projected distance from the highest SB center relative to the line-of-sight. In the model, we 'rotate' the grid for each photon so all escape in the same direction.

[19] Here we selected eight red-peak dominated spectra that are close to the Lyα SB center (i.e. spectrum 11) from the south high SB region: spectra 5, 6, 7, 9, 10, 11, 12, 13.

[20] Specifically, the geometric distance between spectra 9 and 10 in the model is $0.3\,b_{\rm max}$, and the actual physical distance between these two locations are 9.9 kpc. Hence $b_{\rm max} = 33\,{\rm kpc}$.

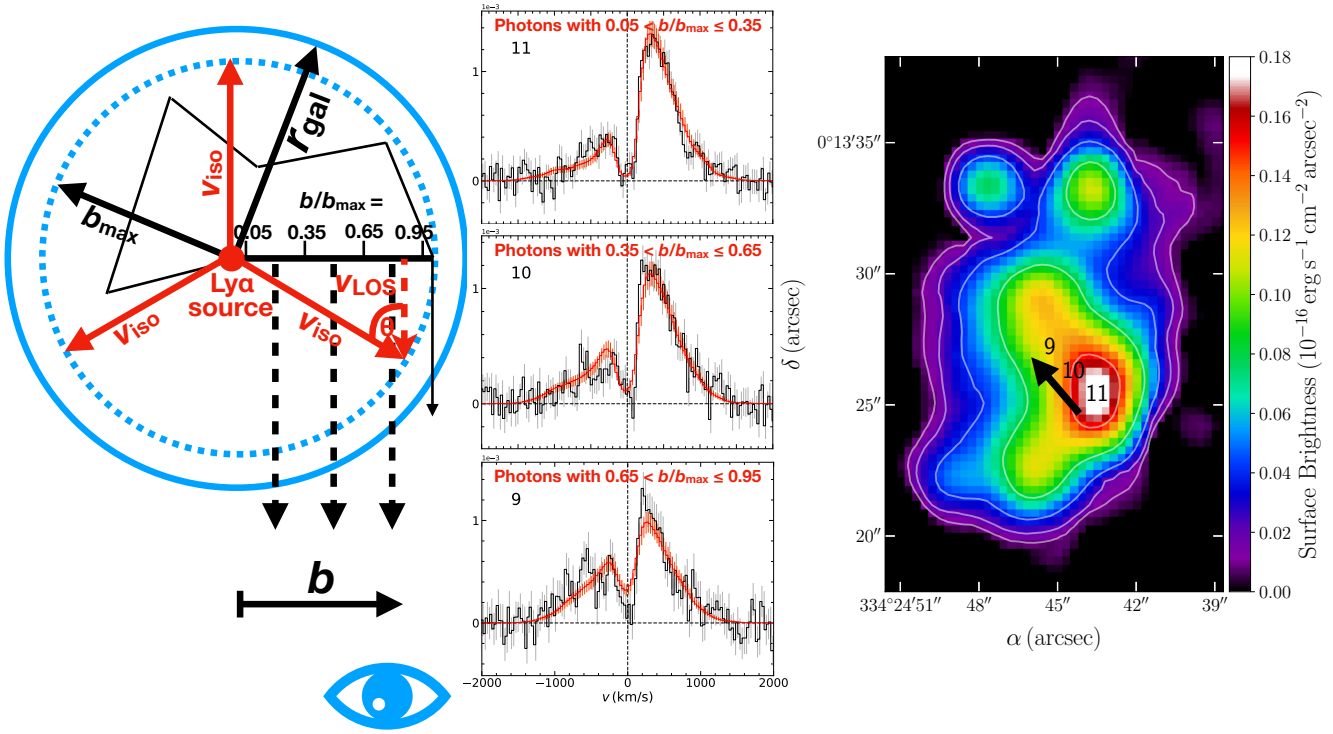

Figure 5. Results of fitting spatially-resolved Lyα spectra (9, 10 and 11) at different impact parameters simultaneously. *Left:* Illustration of how different photon bins are constructed in the multiphase, clumpy model. The ranges of impact parameters of three different Lyα photon bins are: $0.05 < b/b_{\rm max} \leq 0.35$, $0.35 < b/b_{\rm max} \leq 0.65$ and $0.65 < b/b_{\rm max} \leq 0.95$, where $b_{\rm max}$ is the largest impact parameter of all the scattered Lyα photons. The solid red arrows represent an isotropic outflow of the cool clumps with velocity $v_{\rm iso}$, and the dashed red arrow represents the observed clump outflow velocity projected along the line-of-sight, $v_{\rm LOS}$. *Middle:* Three aligned and equally-spaced Lyα spectra (black, with grey 1-σ error bars) and the corresponding binned best-fits (red, with orange 1-σ Poisson errors). The likelihoods of the binned fits are comparable to those of the individual fits. *Right:* The Lyα SB map, with the alignment of three modeled spectra indicated by a black arrow.

Optical: Steidel et al. (2000) first discovered LAB2 using narrow-band imaging and provided its angular size ($\sim 15''$), Lyα luminosity ($\sim 9.0 \times 10^{43}$ erg s^{-1}) and limits on the rest-frame equivalent width ($\gtrsim 370$ Å). They also identified a velocity shear of ~ 2000 km s^{-1} with respect to the LBG, M14.

Wilman et al. (2005) carried out IFU observations using SAURON on the 4.2 m William Herschel Telescope (WHT) on La Palma. They observed the ubiquitous 'double-peak + central trough' feature of most Lyα profiles in LAB2, and modeled the profiles with a Gaussian emission line and a superimposed Voigt profile absorber. They claimed that the profiles can be explained by an 'intrinsic Lyα emission + H I shell absorption' model, where the shell is the cool material swept-up by starburst-driven outflows ('superwinds'). They also noted that a large foreground absorber that covers the whole blob is unlikely, as the absorber would have an unreasonably large size.

Martin et al. (2014) made further IFU observations using the Palomar Cosmic Web Imager (PCWI). They proposed that the Lyα emission could be produced by either AGN fluorescence or gravitational cooling radiation. They also claimed that there is evidence of both inflows and outflows at different viewing angles, which is consistent with our findings that both blue-dominated and red-dominated Lyα profiles exist in LAB2.

X-ray: Basu-Zych & Scharf (2004) first detected an obscured hard X-ray source in the *Chandra* 2 – 8 keV band. They claimed that the unabsorbed X-ray luminosity ($\sim 10^{44}$ erg s^{-1}) is consistent with an AGN. Deeper *Chandra* observations have been carried out in Lehmer et al. (2009a,b), based on which Geach et al. (2009) claimed that the UV luminosity of the AGN alone is sufficient to power the whole blob via photoionization. However, as we have shown in Figure 1 and subsequent analyses, the location of the AGN with respect to the Lyα emission is difficult to reconcile with the Lyα morphology.

IR: Geach et al. (2007) carried out *Spitzer* observations at IRAC (3.6 – 8 μm) and MIPS (24 μm). They reported detections at three positions in LAB2 (named a, b and c), where b is likely the counterpart of the X-ray source, and c is a foreground source at lower redshift[21]. Webb et al. (2009) further confirmed the detection of a and b in the IRAC bands, and we have marked their positions in Figure 1.

Submm: Chapman et al. (2001) first reported a 3.3 ± 1.2 mJy detection at 850 μm within the $\sim 15''$ beam of SCUBA. Geach et al. (2005) studied the relation between the Lyα luminiosity and the bolometric luminosity of 23 LABs and noted that LAB2 is an outlier of the relation, which could be due to the effect of AGN and other environmental factors. However, a recent study by Hine et al. (2016b) reported a non-detection at 850 μm using SCUBA-2. Another recent study by Ao et al. (2017) reported a significant 0.91 ± 0.10 mJy detection at 850 μm using ALMA, which coincides with the X-ray detection from Lehmer et al. (2009a).

Previous studies on LAB2 focused mainly on qualitatively studying the continuum sources (e.g. the LBG M14 and the X-ray source) in terms of their energy budgets and/or analysing the observed Lyα profiles with empirical tools without carrying out ra-

[21] We found that detection c is close to the position where the Lyα SB is the highest (see the left panel of Figure 1). Unfortunately, its mid-IR colors suggest that it should be a foreground galaxy at $z < 1$ (Geach et al. 2007; Webb et al. 2009). In our KCWI datacube, the location of its Ca II H and K lines suggests a redshift of $z = 0.213$.

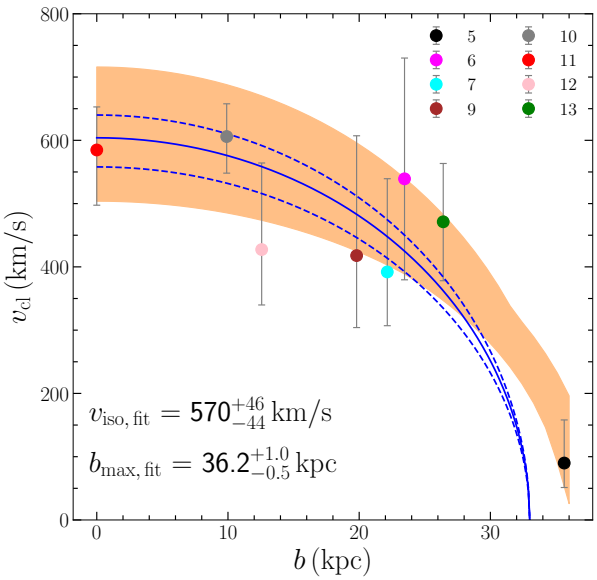

Figure 6. The relation between the clump outflow velocity ($v_{\rm cl}$) and the impact parameter (b). The color-coded points represent $v_{\rm cl}$ values (with 1-σ error bars shown in grey) derived from individual fits of eight different Lyα spectra from the south high SB region, and the orange shaded region represent the range of twenty best-fits (using Eq. 6) of the data points perturbed by their 1-σ uncertainties. The best-fit parameters with 1-σ uncertainties are also shown in the lower left. The blue solid and dashed curves are reference $v_{\rm cl}$ v.s. b curves generated by setting $v_{\rm iso} = 604^{+36}_{-46}$ km s^{-1} (derived from the combined fit) and $b_{\rm max} = 33$ kpc (calculated by mapping the geometric distances in the model to the actual physical distances in Eq. 6). The reference $v_{\rm cl}$ v.s. b curve from the combined fit is fairly consistent with the $v_{\rm cl}$ values derived from individual fits (as well as the fitted $v_{\rm iso}$ and $b_{\rm max}$ values) within 1-σ uncertainties, suggesting the variations in $v_{\rm cl}$ may be simply the projection of a radial outflow along the line-of-sight.

diative transfer calculations. In contrast, the present work carefully examines the spatially-resolved Lyα profiles (such as mapping their blue-to-red flux ratios, see §3.2) and decodes them using radiative transfer calculations with multiphase, clumpy models (see §5). In our modelling, we assumed that a central powering source exists near the highest Lyα SB regions, although it is still puzzling that there is no viable continuum source coincident with the Lyα SB peak (see §4). Not only have we successfully reproduced fifteen representative Lyα profiles with realistic physical parameters, but we also managed to fit Lyα profiles at different impact parameters consistently, and explained the observed spatial variation in the $F_{\rm blue}/F_{\rm red}$ ratio and outflow velocity. These results support the 'central powering + scattering' scenario, i.e. the Lyα photons are generated by central powering source(s) and then scatter with outflowing, multiphase H I gas while propagating outwards. We have also observed signatures of accretion of infalling cool gas at the blob outskirts. As we have shown in §5.2, although the infalling of cool gas is responsible for shaping the observed blue-dominated Lyα profiles, its energy contribution is likely to be minor compared to the photo-ionization by central (as yet unidentified) sources.

7 CONCLUSIONS

We present new deep spectroscopic observations of SSA22-LAB2 at $z = 3.1$ using KCWI and MOSFIRE. The main conclusions of our analysis are:

(i) By creating a narrow-band Lyα image, we observed extended Lyα emission in three distinct regions, among which the south region is the largest and has a high Lyα SB center that is far away from known continuum sources;

(ii) We found that the Lyα profiles are dominated by a red peak in regions of high Lyα SB, but tend to be more symmetric and even blue-peak dominated in the low SB outskirts. The median blue-to-red flux ratio is anti-correlated with Lyα SB, which may be due to the decrease of the projected line-of-sight outflow velocity in the periphery of the halo;

(iii) We searched through the two MOSFIRE slits that had been observed near to the highest Lyα SB regions, and found no significant detection of nebular emission within the region of Lyα emission;

(iv) To decode the spatially-resolved Lyα profiles using Monte-Carlo radiative transfer (MCRT) modelling, we used both multiphase, clumpy models and shell models, both of which successfully reproduced the diverse Lyα morphologies. We found significant correlations between parameters of the two different models, and our derived parameters naturally alleviated the previously reported discrepancies between the shell model parameters and data;

(v) We have managed to fit Lyα spectra at different impact parameters simultaneously assuming a common central source. We also found that the variation of the clump outflow velocity with respect to impact parameter can be approximately explained as a simple line-of-sight projection effect of a radial outflow;

(vi) We conclude that our results support the 'central powering +scattering' scenario, i.e. the Lyα photons are generated by a central powering source and then scatter with outflowing, multiphase H I gas while propagating outwards. The infalling of cool gas is responsible for shaping the observed blue-dominated Lyα profiles, but its energy contribution is likely to be minor compared to the photo-ionization by star-forming galaxies and/or AGNs.

ACKNOWLEDGEMENTS

We thank Phil Hopkins for providing computational resources. ZL, CCS and YC acknowledge financial support by NSF grant AST-2009278. YM acknowledges support from JSPS KAKENHI Grant (17H04831, 17KK0098, 19H00697 and 20H01953). The data presented herein were obtained at the W. M. Keck Observatory, which is operated as a scientific partnership among the California Institute of Technology, the University of California and the National Aeronautics and Space Administration. The Observatory was made possible by the generous financial support of the W. M. Keck Foundation. We are also grateful to the dedicated staff of the W.M. Keck Observatory who keep the instruments and telescopes running effectively. MG was supported by NASA through the NASA Hubble Fellowship grant HST-HF2-51409 awarded by the Space Telescope Science Institute, which is operated by the Association of Universities for Research in Astronomy, Inc., for NASA, under contract NAS5-26555. Numerical calculations were run on the Caltech compute cluster "Wheeler," allocations from XSEDE TG-AST130039 and PRAC NSF.1713353 supported by the NSF, and NASA HEC SMD-16-7592. This research made use of Montage. It is funded by the National Science Foundation under Grant Number ACI-1440620, and was previously funded by the National Aeronautics and Space Administration's Earth Science Technology Office, Computation Technologies Project, under Cooperative Agreement Number NCC5-626 between NASA and the California Institute of Technology. We also acknowledge the use of the the following software packages: Astropy (Astropy Collaboration et al. 2018), the SciPy and NumPy system (Virtanen et al. 2020; Harris et al. 2020), seaborn (Waskom 2021) and QFitsView[22].

[22] https://www.mpe.mpg.de/ ott/QFitsView/

DATA AVAILABILITY

The data underlying this article will be shared on reasonable request to the corresponding author.

REFERENCES

Ahn S.-H., Lee H.-W., Lee H. M., 2003, MNRAS, 340, 863
Ajiki M., et al., 2002, ApJ, 576, L25
Ao Y., et al., 2017, ApJ, 850, 178
Ao Y., et al., 2020, Nature Astronomy, 4, 670
Astropy Collaboration et al., 2018, AJ, 156, 123
Bacon R., et al., 2014, The Messenger, 157, 13
Basu-Zych A., Scharf C., 2004, ApJ, 615, L85
Beck M., Scarlata C., Hayes M., Dijkstra M., Jones T. J., 2016, ApJ, 818, 138
Byrohl C., Gronke M., 2020, A&A, 642, L16
Cai Z., et al., 2017, ApJ, 837, 71
Cantalupo S., Porciani C., Lilly S. J., Miniati F., 2005, ApJ, 628, 61
Cantalupo S., Arrigoni-Battaia F., Prochaska J. X., Hennawi J. F., Madau P., 2014, Nature, 506, 63
Chapman S. C., Lewis G. F., Scott D., Richards E., Borys C., Steidel C. C., Adelberger K. L., Shapley A. E., 2001, ApJ, 548, L17
Chen H.-W., Lanzetta K. M., Webb J. K., Barcons X., 2001, ApJ, 559, 654
Chen Y., et al., 2020, MNRAS, 499, 1721
Colbert J. W., Teplitz H., Francis P., Palunas P., Williger G. M., Woodgate B., 2006, ApJ, 637, L89
Daddi E., et al., 2020, arXiv e-prints, p. arXiv:2006.11089
Dawson S., Spinrad H., Stern D., Dey A., van Breugel W., de Vries W., Reuland M., 2002, ApJ, 570, 92
Dey A., et al., 2005, ApJ, 629, 654
Dijkstra M., Kramer R., 2012, MNRAS, 424, 1672
Dijkstra M., Loeb A., 2008, MNRAS, 386, 492
Dijkstra M., Loeb A., 2009, MNRAS, 400, 1109
Dijkstra M., Haiman Z., Spaans M., 2006a, ApJ, 649, 14
Dijkstra M., Haiman Z., Spaans M., 2006b, ApJ, 649, 37
Dopita M. A., Sutherland R. S., 2003, Astrophysics of the diffuse universe
Eide M. B., Gronke M., Dijkstra M., Hayes M., 2018, ApJ, 856, 156
Erb D. K., Bogosavljević M., Steidel C. C., 2011, ApJ, 740, L31
Erb D. K., Steidel C. C., Chen Y., 2018, ApJ, 862, L10
Fardal M. A., Katz N., Gardner J. P., Hernquist L., Weinberg D. H., Davé R., 2001, ApJ, 562, 605
Faucher-Giguère C.-A., Kereš D., Dijkstra M., Hernquist L., Zaldarriaga M., 2010, ApJ, 725, 633
Francis P. J., et al., 1996, ApJ, 457, 490
Furlanetto S. R., Schaye J., Springel V., Hernquist L., 2005, ApJ, 622, 7
Fynbo J. U., Møller P., Warren S. J., 1999, MNRAS, 305, 849
Geach J. E., et al., 2005, MNRAS, 363, 1398
Geach J. E., Smail I., Chapman S. C., Alexand er D. M., Blain A. W., Stott J. P., Ivison R. J., 2007, ApJ, 655, L9
Geach J. E., et al., 2009, ApJ, 700, 1
Goerdt T., Dekel A., Sternberg A., Ceverino D., Teyssier R., Primack J. R., 2010, MNRAS, 407, 613
Gronke M., 2017, A&A, 608, A139
Gronke M., Dijkstra M., 2016, ApJ, 826, 14
Gronke M., Oh S. P., 2018, MNRAS, 480, L111
Gronke M., Bull P., Dijkstra M., 2015, ApJ, 812, 123
Gronke M., Dijkstra M., McCourt M., Oh S. P., 2016, ApJ, 833, L26
Gronke M., Dijkstra M., McCourt M., Peng Oh S., 2017, A&A, 607, A71
Haiman Z., Rees M. J., 2001, ApJ, 556, 87
Haiman Z., Spaans M., Quataert E., 2000, ApJ, 537, L5
Hansen M., Oh S. P., 2006, MNRAS, 367, 979
Harris C. R., et al., 2020, Nature, 585, 357
Hashimoto T., et al., 2015, ApJ, 812, 157
Hayes M., Scarlata C., Siana B., 2011, Nature, 476, 304
Heckman T. M., Armus L., Miley G. K., 1990, ApJS, 74, 833
Hennawi J. F., Prochaska J. X., Kollmeier J., Zheng Z., 2009, ApJ, 693, L49
Herenz E. C., Wisotzki L., 2017, A&A, 602, A111
Hine N. K., Geach J. E., Alexander D. M., Lehmer B. D., Chapman S. C., Matsuda Y., 2016a, MNRAS, 455, 2363
Hine N. K., et al., 2016b, MNRAS, 460, 4075
Keel W. C., Cohen S. H., Windhorst R. A., Waddington I., 1999, AJ, 118, 2547
Kim E., Yang Y., Zabludoff A., Smith P., Jannuzi B., Lee M. G., Hwang N., Park B.-G., 2020, ApJ, 894, 33
Laursen P., Duval F., Östlin G., 2013, ApJ, 766, 124
Leclercq F., et al., 2017, A&A, 608, A8
Leclercq F., et al., 2020, A&A, 635, A82
Lehmer B. D., et al., 2009a, MNRAS, 400, 299
Lehmer B. D., et al., 2009b, ApJ, 691, 687
Li Z., Hopkins P. F., Squire J., Hummels C., 2020, MNRAS, 492, 1841
Li Z., Steidel C. C., Gronke M., Chen Y., 2021, MNRAS, 502, 2389
Martin D. C., Chang D., Matuszewski M., Morrissey P., Rahman S., Moore A., Steidel C. C., Matsuda Y., 2014, ApJ, 786, 107
Matsuda Y., et al., 2004, AJ, 128, 569
Matsuda Y., et al., 2011, MNRAS, 410, L13
McCourt M., Oh S. P., O'Leary R., Madigan A.-M., 2018, MNRAS, 473, 5407
McLean I. S., et al., 2010, in Proc. SPIE. p. 77351E, doi:10.1117/12.856715
McLean I. S., et al., 2012, in Proc. SPIE. p. 84460J, doi:10.1117/12.924794
McQuinn M., 2016, ARA&A, 54, 313
Mori M., Umemura M., Ferrara A., 2004, ApJ, 613, L97
Morrissey P., et al., 2018, ApJ, 864, 93
Nestor D. B., Shapley A. E., Kornei K. A., Steidel C. C., Siana B., 2013, ApJ, 765, 47
Neufeld D. A., 1991, ApJ, 370, L85
Nilsson K. K., Fynbo J. P. U., Møller P., Sommer-Larsen J., Ledoux C., 2006, A&A, 452, L23
Orlitová I., Verhamme A., Henry A., Scarlata C., Jaskot A., Oey M. S., Schaerer D., 2018, A&A, 616, A60
Ouchi M., et al., 2009, ApJ, 696, 1164
Planck Collaboration et al., 2018, arXiv e-prints, p. arXiv:1807.06209
Prescott M. K. M., Kashikawa N., Dey A., Matsuda Y., 2008, ApJ, 678, L77
Prescott M. K. M., Dey A., Jannuzi B. T., 2009, ApJ, 702, 554
Prescott M. K. M., Dey A., Jannuzi B. T., 2012, ApJ, 748, 125
Prochaska J. X., Weiner B., Chen H. W., Mulchaey J., Cooksey K., 2011, ApJ, 740, 91
Rosdahl J., Blaizot J., 2012, MNRAS, 423, 344
Rudie G. C., et al., 2012, ApJ, 750, 67
Saito T., Shimasaku K., Okamura S., Ouchi M., Akiyama M., Yoshida M., 2006, ApJ, 648, 54
Saito T., Shimasaku K., Okamura S., Ouchi M., Akiyama M., Yoshida M., Ueda Y., 2008, ApJ, 675, 1076
Scannapieco E., Brüggen M., 2015, ApJ, 805, 158
Skilling J., 2004, in Fischer R., Preuss R., Toussaint U. V., eds, American Institute of Physics Conference Series Vol. 735, American Institute of Physics Conference Series. pp 395–405, doi:10.1063/1.1835238
Skilling J., 2006, Bayesian Anal., 1, 833
Smith D. J. B., Jarvis M. J., 2007, MNRAS, 378, L49
Smith D. J. B., Jarvis M. J., Lacy M., Martínez-Sansigre A., 2008, MNRAS, 389, 799
Sparre M., Pfrommer C., Ehlert K., 2020, MNRAS, 499, 4261
Speagle J. S., 2020, MNRAS, 493, 3132
Steidel C. C., Adelberger K. L., Dickinson M., Giavalisco M., Pettini M., Kellogg M., 1998, ApJ, 492, 428
Steidel C. C., Adelberger K. L., Shapley A. E., Pettini M., Dickinson M., Giavalisco M., 2000, ApJ, 532, 170
Steidel C. C., Adelberger K. L., Shapley A. E., Pettini M., Dickinson M., Giavalisco M., 2003, ApJ, 592, 728
Steidel C. C., Erb D. K., Shapley A. E., Pettini M., Reddy N., Bogosavljević M., Rudie G. C., Rakic O., 2010, ApJ, 717, 289
Steidel C. C., Bogosavljević M., Shapley A. E., Kollmeier J. A., Reddy N. A., Erb D. K., Pettini M., 2011, ApJ, 736, 160
Steidel C. C., et al., 2014, ApJ, 795, 165
Strom A. L., Steidel C. C., Rudie G. C., Trainor R. F., Pettini M., Reddy N. A., 2017, ApJ, 836, 164
Taniguchi Y., Shioya Y., 2000, ApJ, 532, L13
Taniguchi Y., Shioya Y., Kakazu Y., 2001, ApJ, 562, L15
Trebitsch M., Verhamme A., Blaizot J., Rosdahl J., 2016, A&A, 593, A122
Tumlinson J., et al., 2013, ApJ, 777, 59
Tumlinson J., Peeples M. S., Werk J. K., 2017, ARA&A, 55, 389
Verhamme A., Schaerer D., Maselli A., 2006, A&A, 460, 397

Virtanen P., et al., 2020, Nature Methods, 17, 261
Waskom M. L., 2021, Journal of Open Source Software, 6, 3021
Webb T. M. A., Yamada T., Huang J. S., Ashby M. L. N., Matsuda Y., Egami E., Gonzalez M., Hayashimo T., 2009, ApJ, 692, 1561
Wilman R. J., Gerssen J., Bower R. G., Morris S. L., Bacon R., de Zeeuw P. T., Davies R. L., 2005, Nature, 436, 227
Wisotzki L., et al., 2016, A&A, 587, A98
Wisotzki L., et al., 2018, Nature, 562, 229
Yang Y., Zabludoff A., Tremonti C., Eisenstein D., Davé R., 2009, ApJ, 693, 1579
Yang Y., Zabludoff A., Eisenstein D., Davé R., 2010, ApJ, 719, 1654
Zheng Z., Miralda-Escudé J., 2002, ApJ, 578, 33

APPENDIX A: POSTERIOR PROBABILITY DISTRIBUTIONS OF THE MULTIPHASE, CLUMPY MODEL PARAMETERS

Here we present the joint and marginal posterior probability distributions of the multiphase, clumpy model parameters for all fifteen representative Lyα spectra derived from nested sampling.

This paper has been typeset from a TEX/LATEX file prepared by the author.

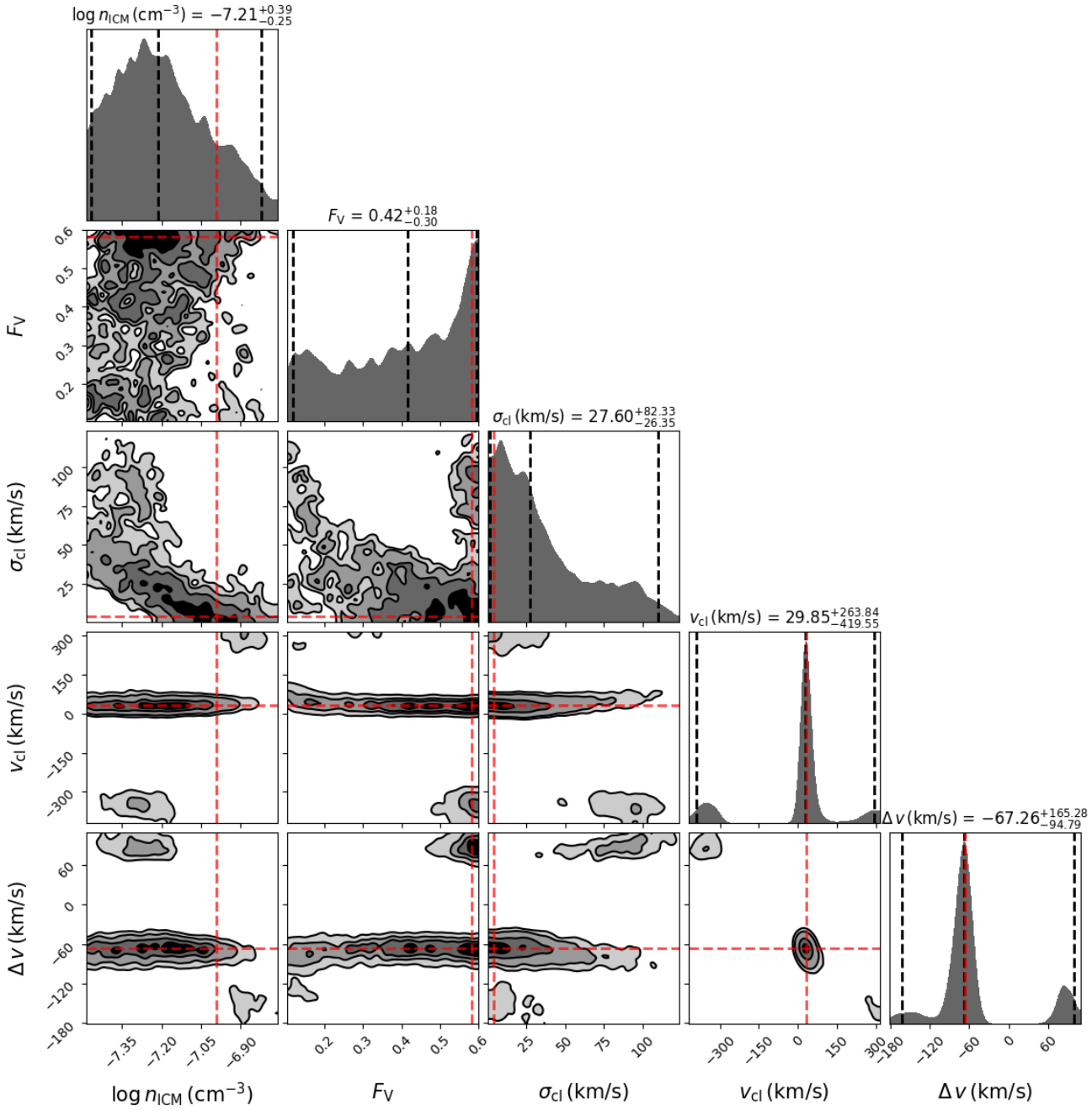
log $n_{\rm ICM}$ (cm^{-3}) = $-7.21^{+0.39}_{-0.25}$
$F_{\rm V}$ = $0.42^{+0.18}_{-0.30}$
$\sigma_{\rm cl}$ (km/s) = $27.60^{+82.33}_{-26.35}$
$v_{\rm cl}$ (km/s) = $29.85^{+263.84}_{-419.55}$
Δv (km/s) = $-67.26^{+165.28}_{-94.79}$
log $n_{\rm ICM}$ (cm^{-3})
$F_{\rm V}$
$\sigma_{\rm cl}$ (km/s)
$v_{\rm cl}$ (km/s)
Δv (km/s)

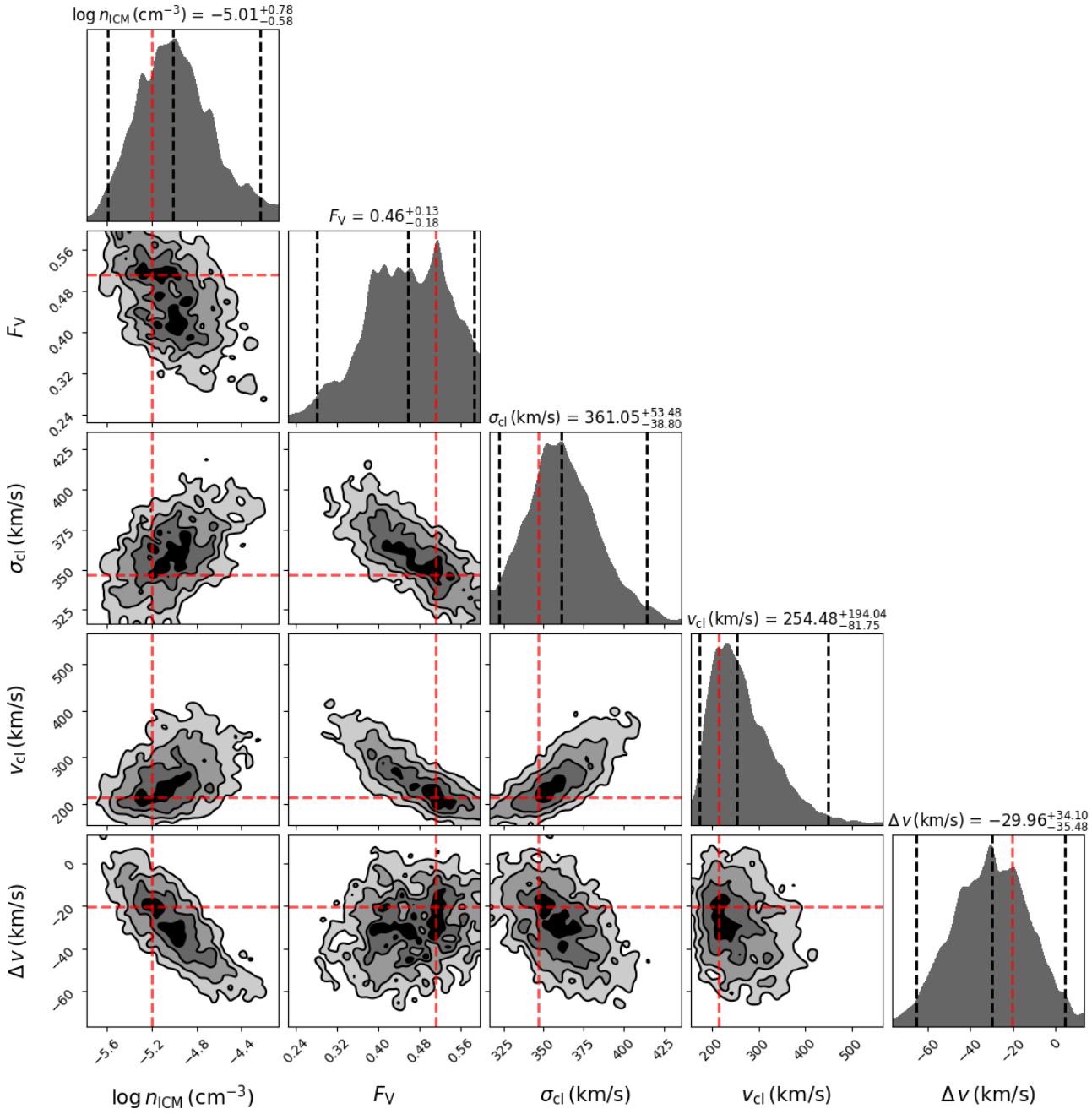
log $n_{\rm ICM}$ (cm^{-3}) = $-5.01^{+0.78}_{-0.58}$
$F_{\rm V}$ = $0.46^{+0.13}_{-0.18}$
$\sigma_{\rm cl}$ (km/s) = $361.05^{+53.48}_{-38.80}$
$v_{\rm cl}$ (km/s) = $254.48^{+194.04}_{-81.75}$
Δv (km/s) = $-29.96^{+34.10}_{-35.48}$
log $n_{\rm ICM}$ (cm^{-3})
$F_{\rm V}$
$\sigma_{\rm cl}$ (km/s)
$v_{\rm cl}$ (km/s)
Δv (km/s)

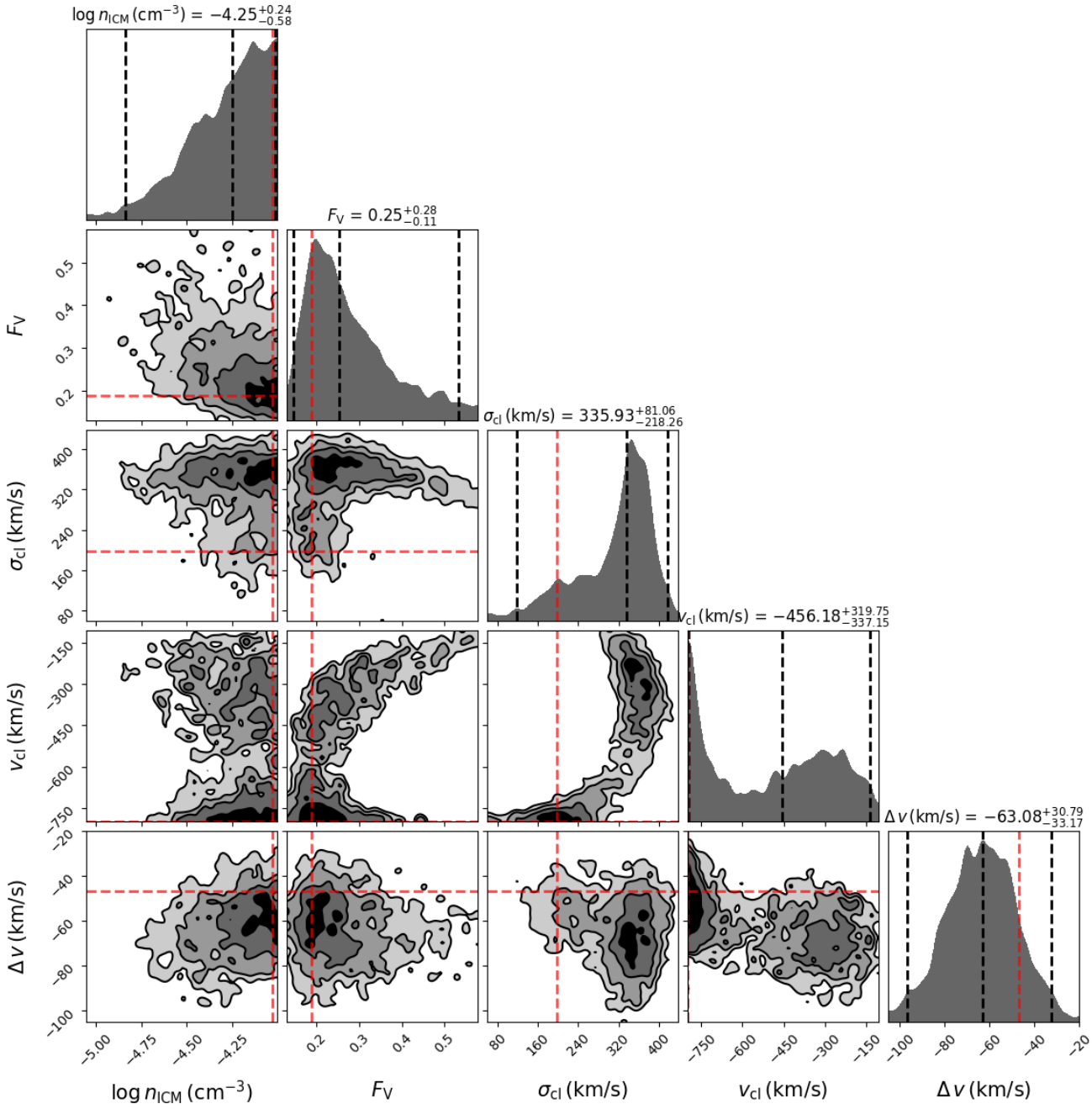
log n_{ICM} (cm^{-3}) = $-4.25^{+0.24}_{-0.58}$
F_V = $0.25^{+0.28}_{-0.11}$
σ_{cl} (km/s) = $335.93^{+81.06}_{-218.26}$
v_{cl} (km/s) = $-456.18^{+319.75}_{-337.15}$
Δv (km/s) = $-63.08^{+30.79}_{-33.17}$
log n_{ICM} (cm^{-3})
F_V
σ_{cl} (km/s)
v_{cl} (km/s)
Δv (km/s)

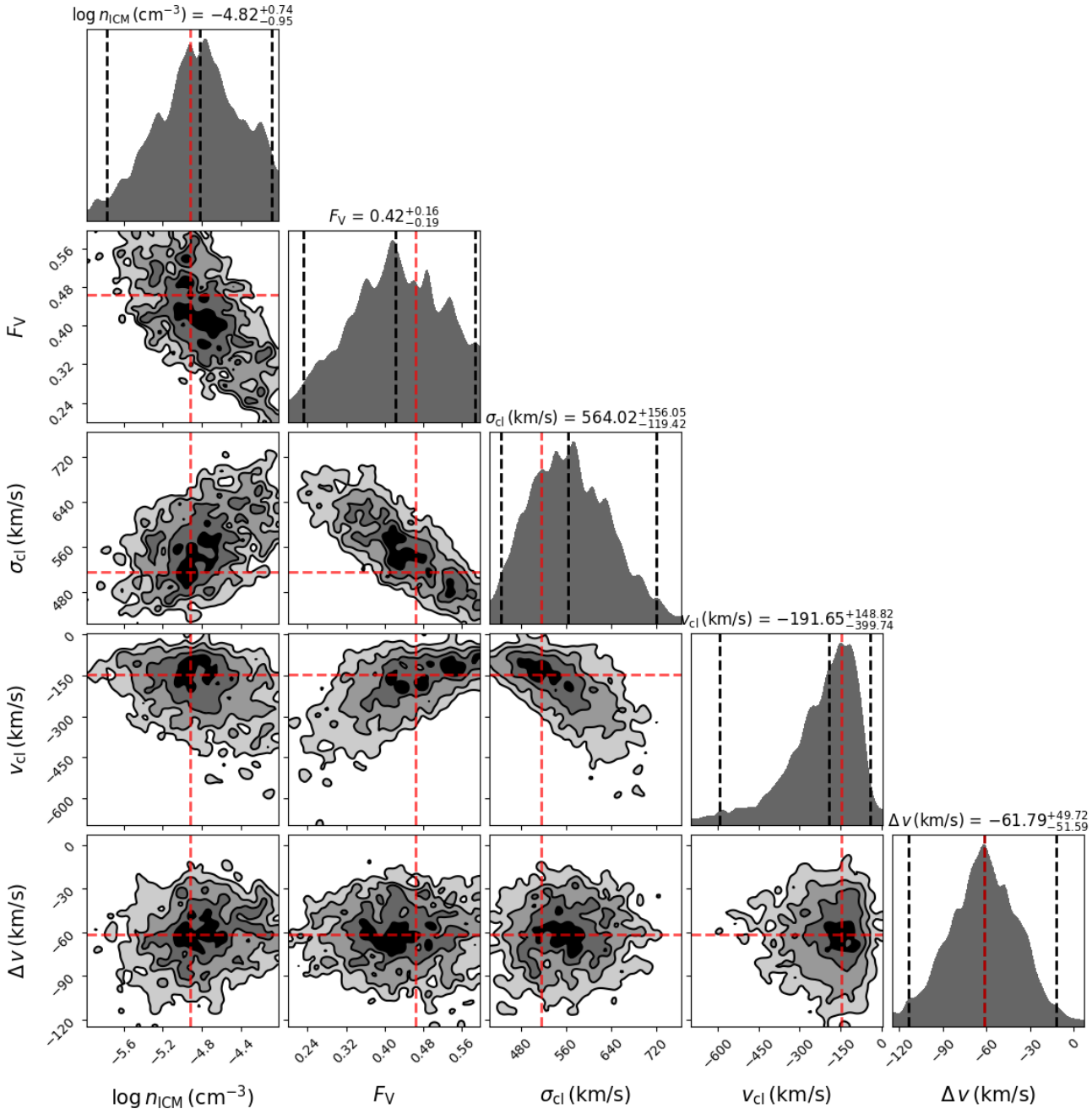
log n_{ICM} (cm^{-3}) = $-4.82^{+0.74}_{-0.95}$
F_V = $0.42^{+0.16}_{-0.19}$
σ_{cl} (km/s) = $564.02^{+156.05}_{-119.42}$
v_{cl} (km/s) = $-191.65^{+148.82}_{-399.74}$
Δv (km/s) = $-61.79^{+49.72}_{-51.59}$
log n_{ICM} (cm^{-3})
F_V
σ_{cl} (km/s)
v_{cl} (km/s)
Δv (km/s)

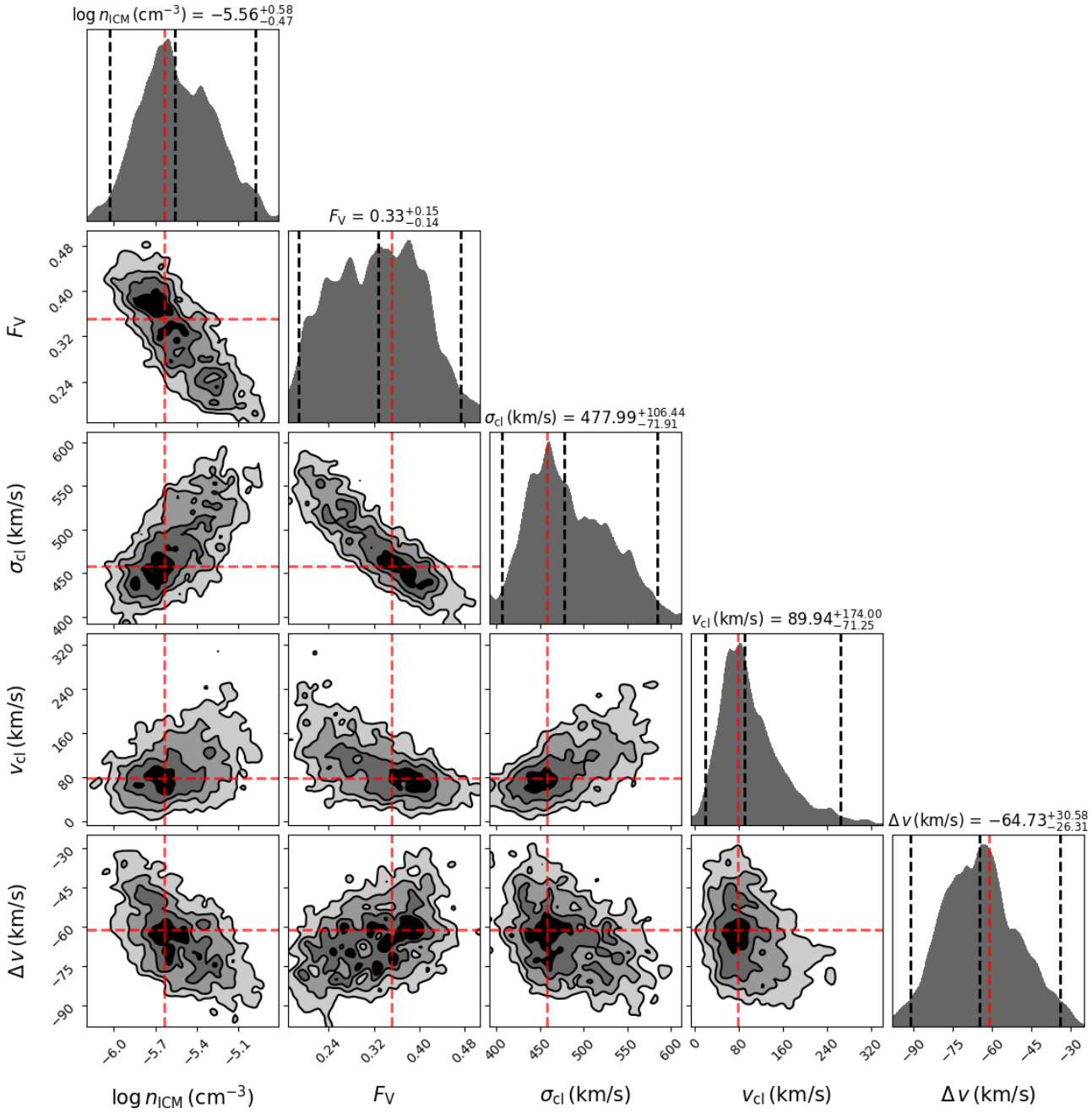
log $n_{\rm ICM}$ (cm^{-3}) = $-5.56^{+0.58}_{-0.47}$
$F_{\rm V}$ = $0.33^{+0.15}_{-0.14}$
$\sigma_{\rm cl}$ (km/s) = $477.99^{+106.44}_{-71.91}$
$v_{\rm cl}$ (km/s) = $89.94^{+174.00}_{-71.25}$
Δv (km/s) = $-64.73^{+30.58}_{-26.31}$
log $n_{\rm ICM}$ (cm^{-3})
$F_{\rm V}$
$\sigma_{\rm cl}$ (km/s)
$v_{\rm cl}$ (km/s)
Δv (km/s)

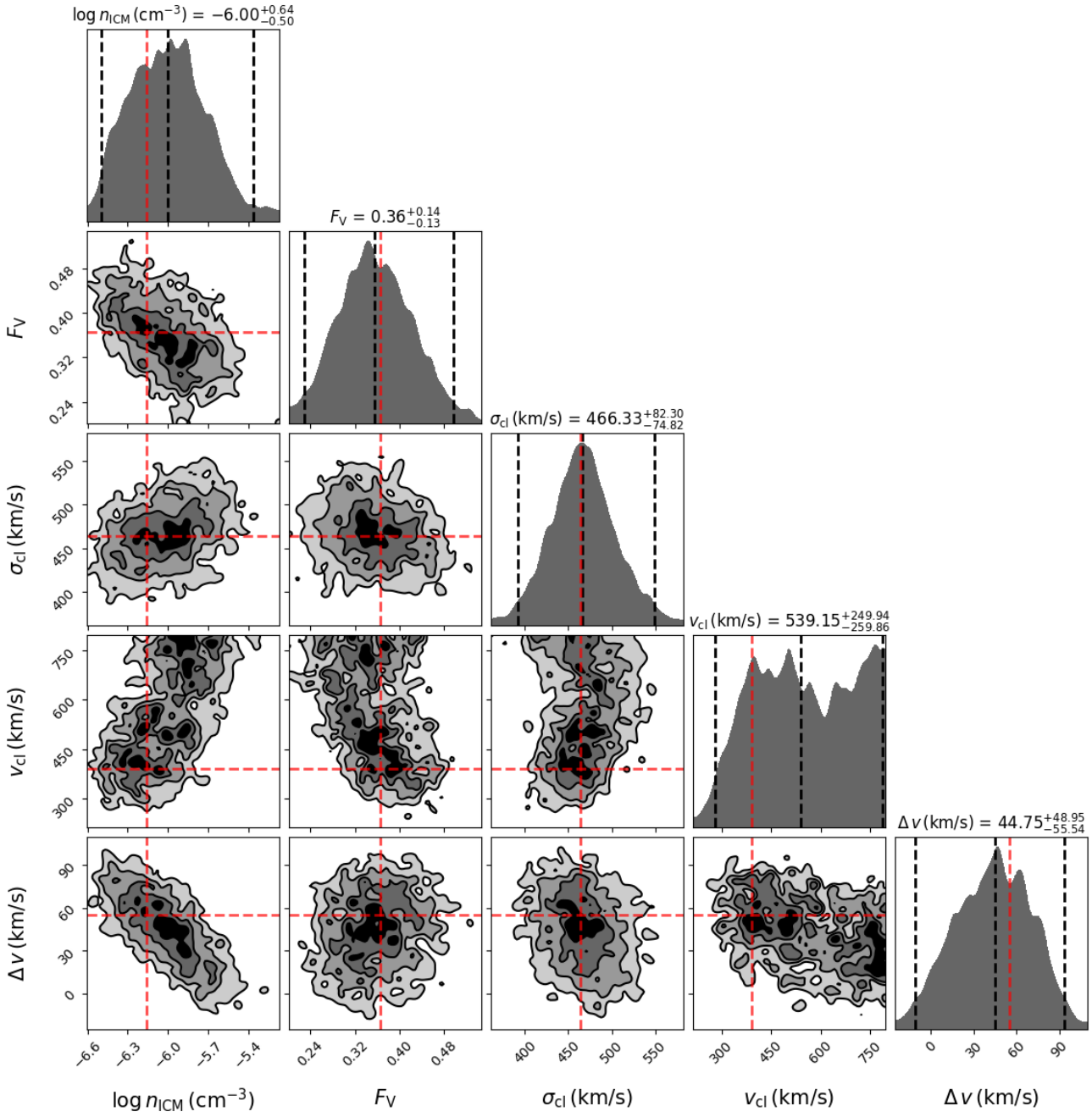
log n_{ICM} (cm^{-3}) = $-6.00^{+0.64}_{-0.50}$
F_V = $0.36^{+0.14}_{-0.13}$
σ_{cl} (km/s) = $466.33^{+82.30}_{-74.82}$
v_{cl} (km/s) = $539.15^{+249.94}_{-259.86}$
Δv (km/s) = $44.75^{+48.95}_{-55.54}$
log n_{ICM} (cm^{-3})
F_V
σ_{cl} (km/s)
v_{cl} (km/s)
Δv (km/s)

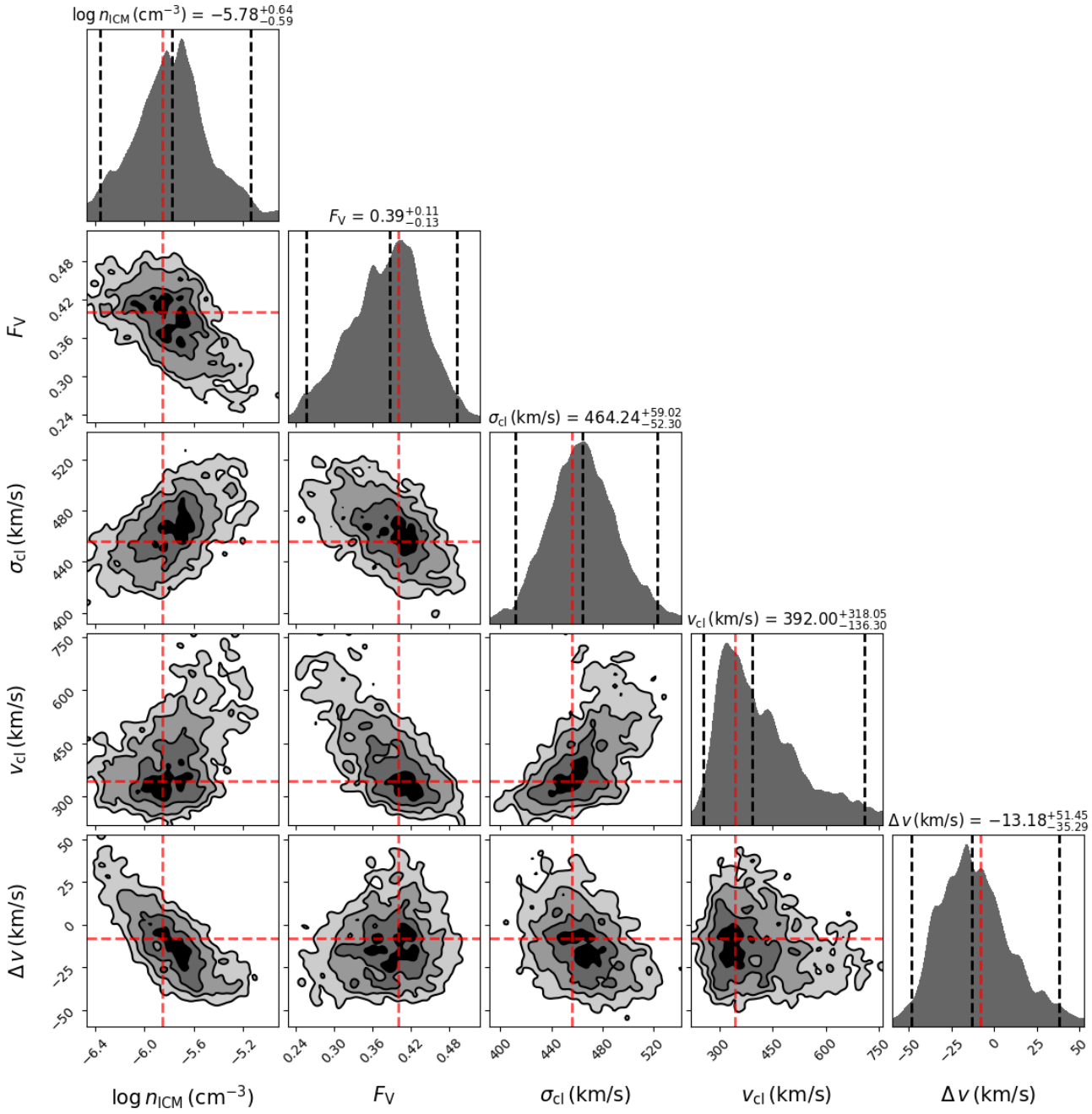
log $n_{\rm ICM}$ (cm^{-3}) = $-5.78^{+0.64}_{-0.59}$
$F_{\rm V}$ = $0.39^{+0.11}_{-0.13}$
$\sigma_{\rm cl}$ (km/s) = $464.24^{+59.02}_{-52.30}$
$v_{\rm cl}$ (km/s) = $392.00^{+318.05}_{-136.30}$
Δv (km/s) = $-13.18^{+51.45}_{-35.29}$
log $n_{\rm ICM}$ (cm^{-3})
$F_{\rm V}$
$\sigma_{\rm cl}$ (km/s)
$v_{\rm cl}$ (km/s)
Δv (km/s)

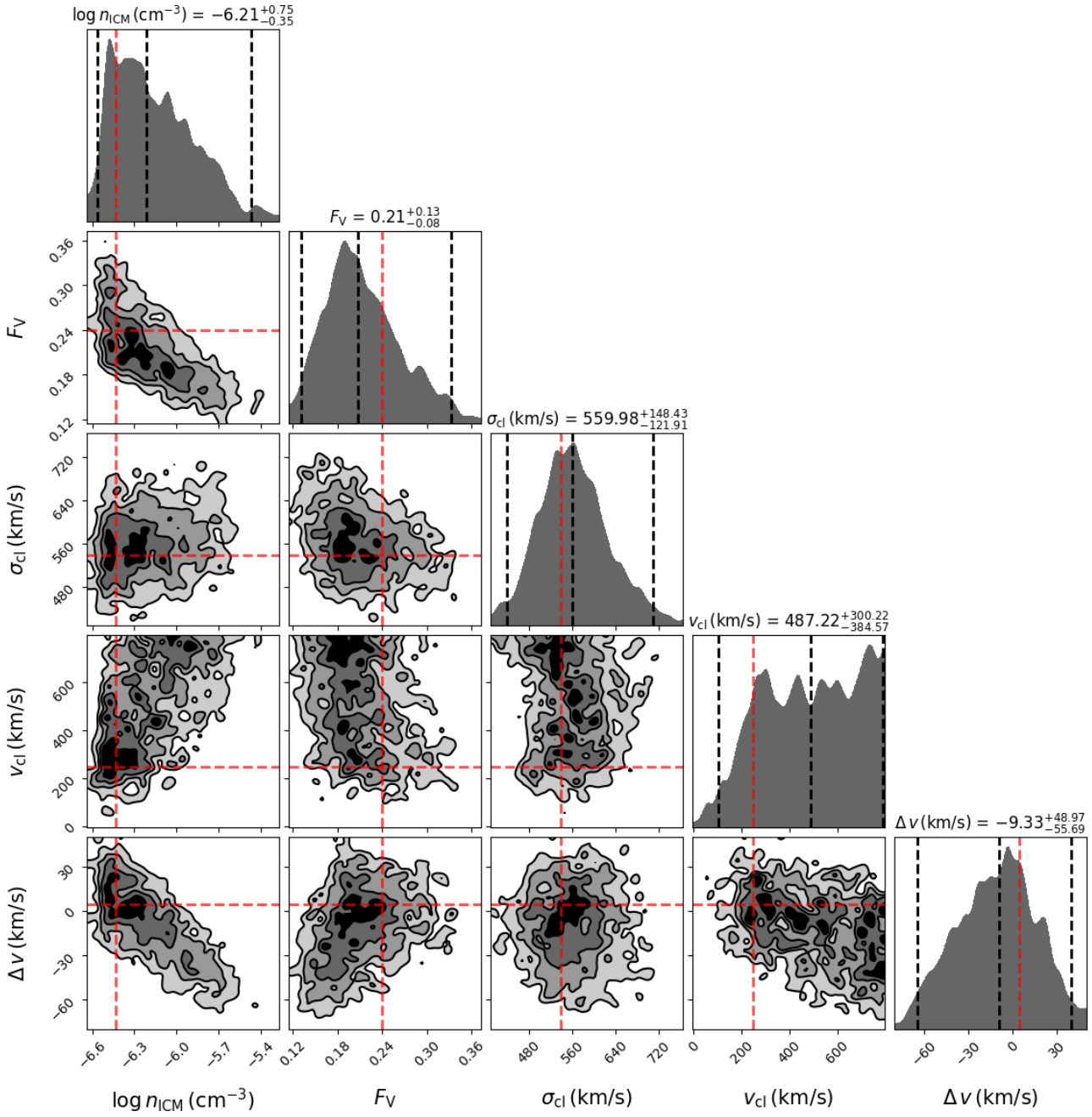
log n_{ICM} (cm^{-3}) = $-6.21^{+0.75}_{-0.35}$
F_V = $0.21^{+0.13}_{-0.08}$
σ_{cl} (km/s) = $559.98^{+148.43}_{-121.91}$
v_{cl} (km/s) = $487.22^{+300.22}_{-384.57}$
Δv (km/s) = $-9.33^{+48.97}_{-55.69}$
log n_{ICM} (cm^{-3})
F_V
σ_{cl} (km/s)
v_{cl} (km/s)
Δv (km/s)

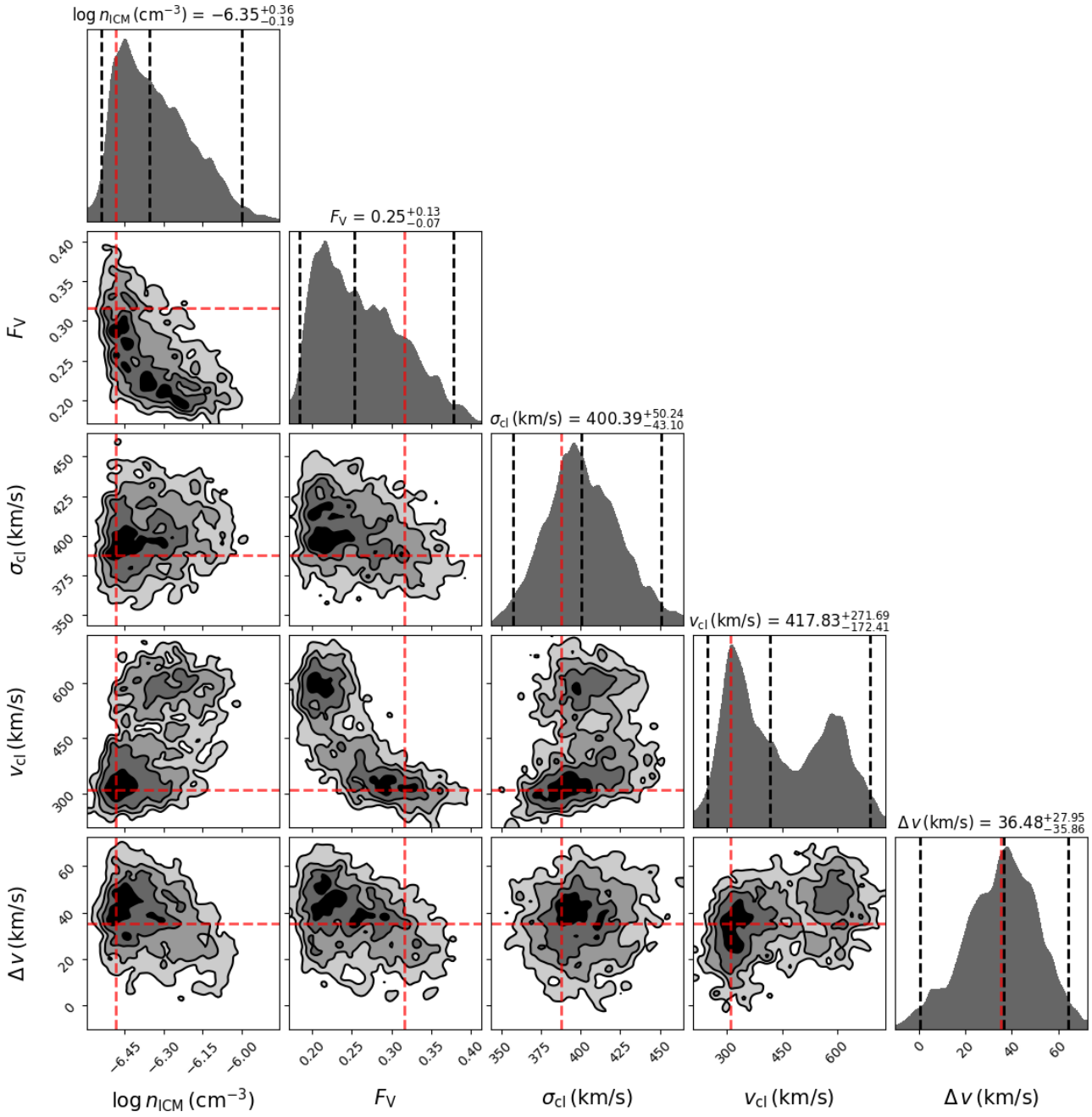
log $n_{\rm ICM}$ (cm^{-3}) = $-6.35^{+0.36}_{-0.19}$
$F_{\rm V}$ = $0.25^{+0.13}_{-0.07}$
$\sigma_{\rm cl}$ (km/s) = $400.39^{+50.24}_{-43.10}$
$v_{\rm cl}$ (km/s) = $417.83^{+271.69}_{-172.41}$
Δv (km/s) = $36.48^{+27.95}_{-35.86}$
log $n_{\rm ICM}$ (cm^{-3})
$F_{\rm V}$
$\sigma_{\rm cl}$ (km/s)
$v_{\rm cl}$ (km/s)
Δv (km/s)

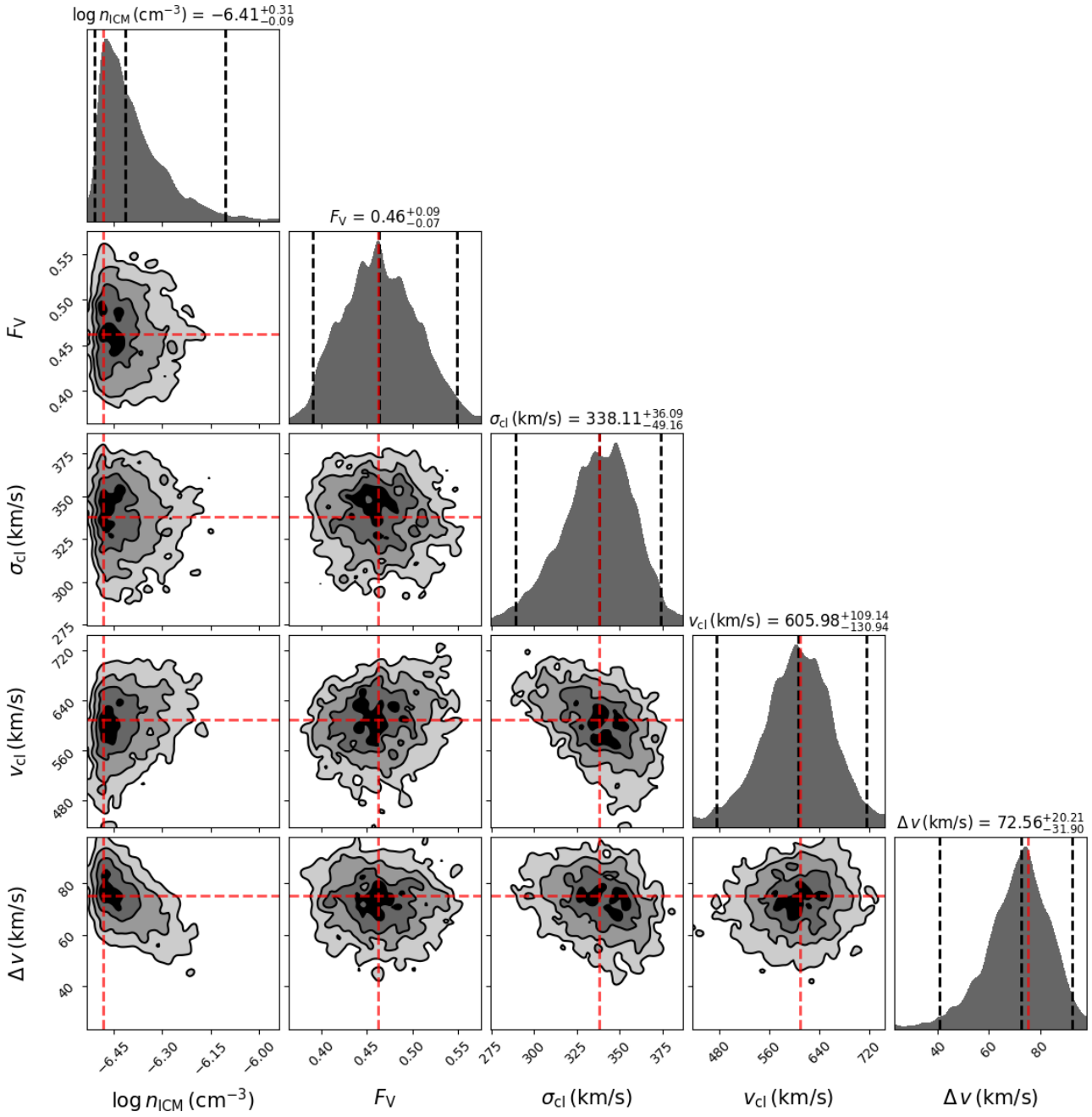
log n_{ICM} (cm^{-3}) = $-6.41^{+0.31}_{-0.09}$
F_V = $0.46^{+0.09}_{-0.07}$
σ_{cl} (km/s) = $338.11^{+36.09}_{-49.16}$
v_{cl} (km/s) = $605.98^{+109.14}_{-130.94}$
Δv (km/s) = $72.56^{+20.21}_{-31.90}$
log n_{ICM} (cm^{-3})
F_V
σ_{cl} (km/s)
v_{cl} (km/s)
Δv (km/s)

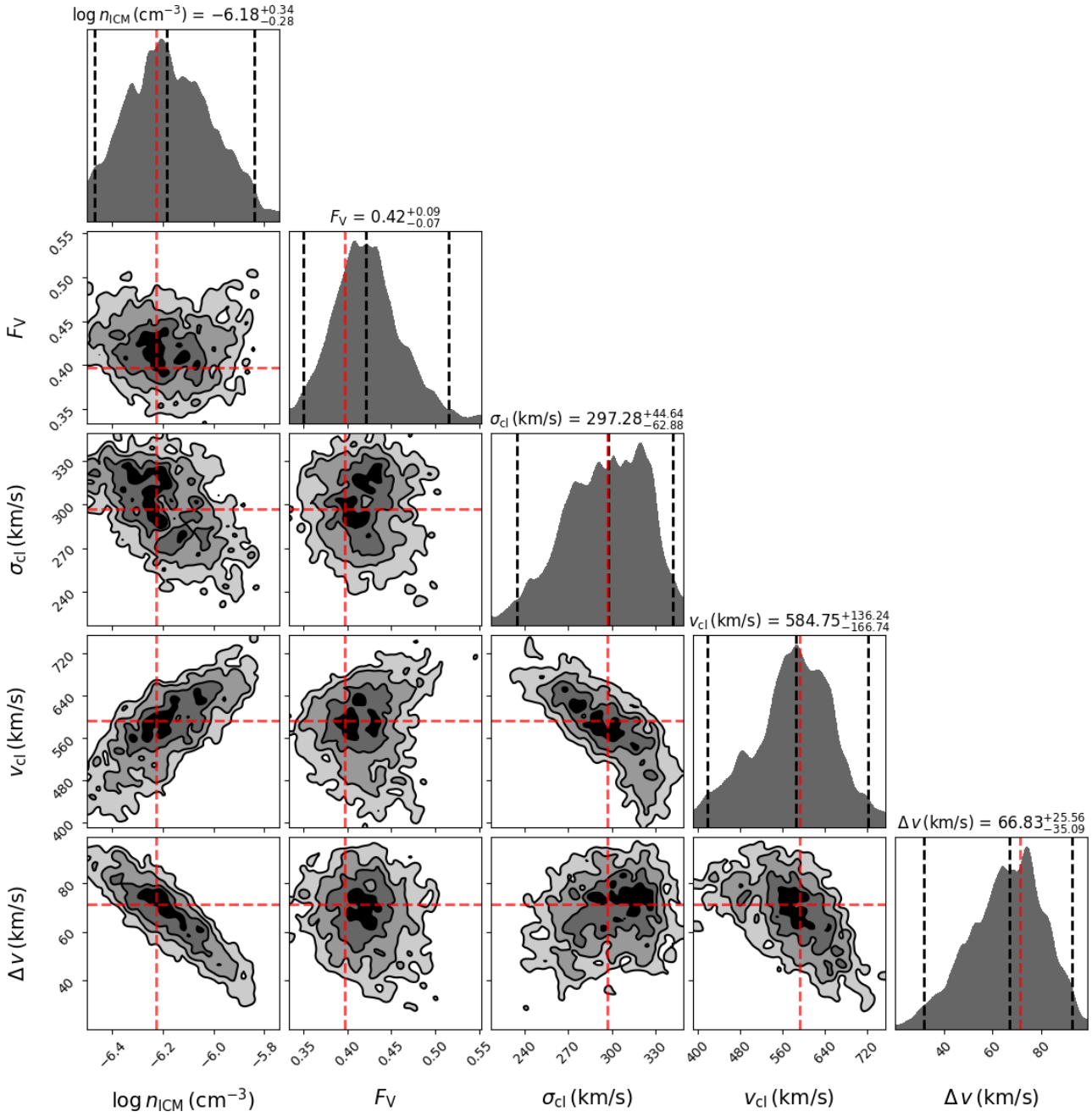
log n_{ICM} (cm^{-3}) = $-6.18^{+0.34}_{-0.28}$
F_V = $0.42^{+0.09}_{-0.07}$
σ_{cl} (km/s) = $297.28^{+44.64}_{-62.88}$
v_{cl} (km/s) = $584.75^{+136.24}_{-166.74}$
Δv (km/s) = $66.83^{+25.56}_{-35.09}$
log n_{ICM} (cm^{-3})
F_V
σ_{cl} (km/s)
v_{cl} (km/s)
Δv (km/s)

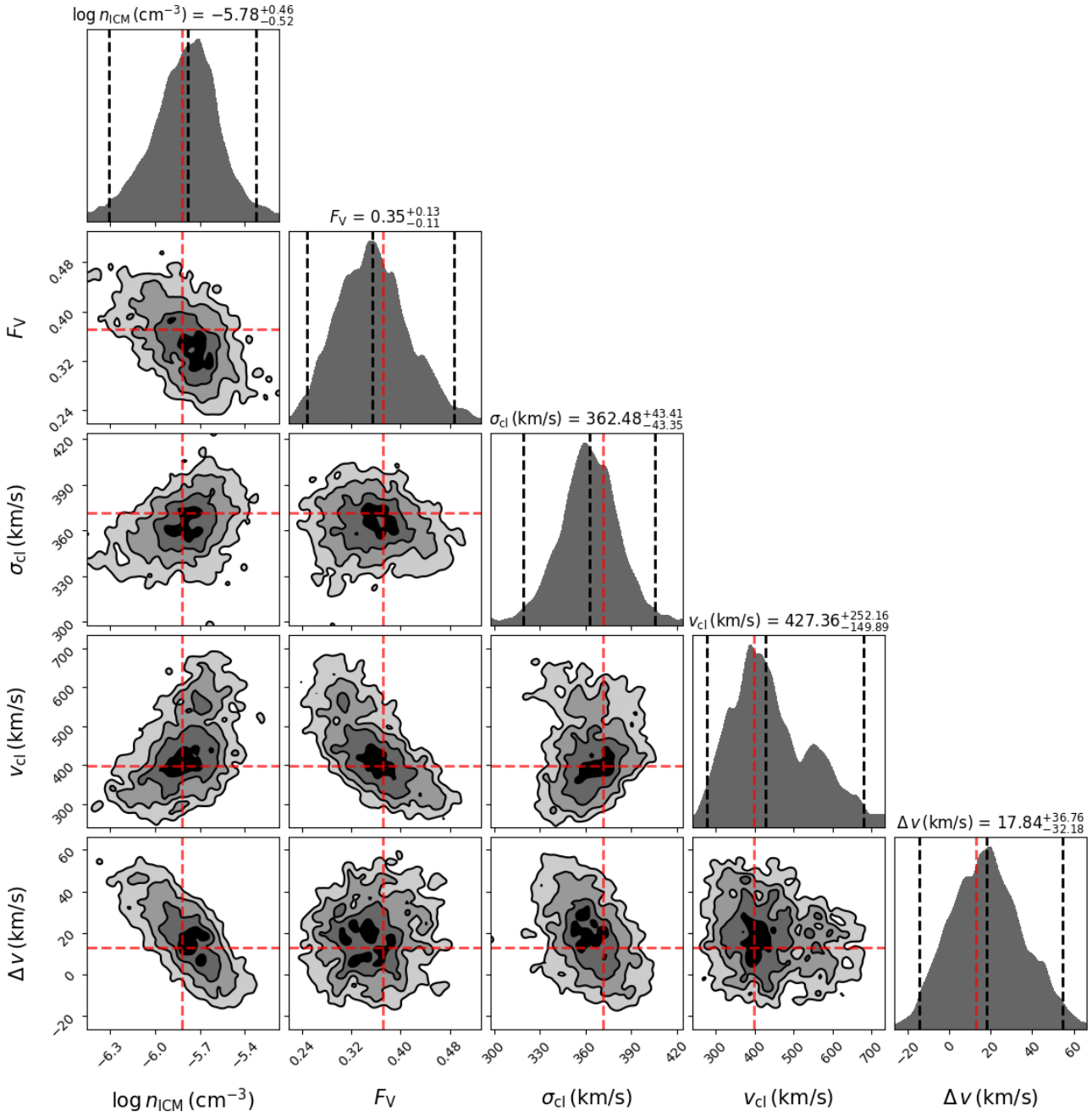
log n_{ICM} (cm^{-3}) = $-5.78^{+0.46}_{-0.52}$
F_V = $0.35^{+0.13}_{-0.11}$
σ_{cl} (km/s) = $362.48^{+43.41}_{-43.35}$
v_{cl} (km/s) = $427.36^{+252.16}_{-149.89}$
Δv (km/s) = $17.84^{+36.76}_{-32.18}$
log n_{ICM} (cm^{-3})
F_V
σ_{cl} (km/s)
v_{cl} (km/s)
Δv (km/s)

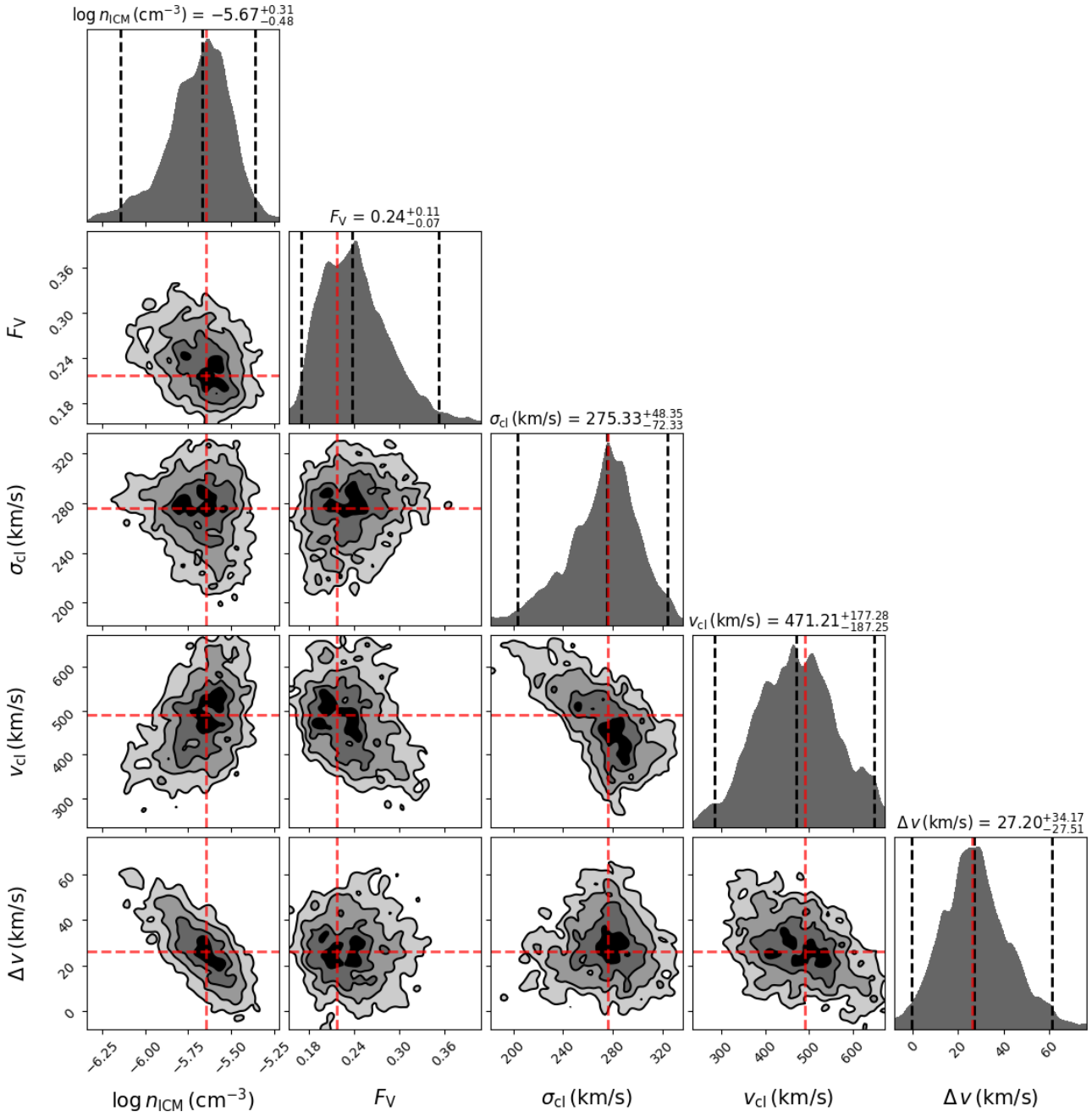
log $n_{\rm ICM}$ (cm^{-3}) = $-5.67^{+0.31}_{-0.48}$
$F_{\rm V}$ = $0.24^{+0.11}_{-0.07}$
$\sigma_{\rm cl}$ (km/s) = $275.33^{+48.35}_{-72.33}$
$v_{\rm cl}$ (km/s) = $471.21^{+177.28}_{-187.25}$
Δv (km/s) = $27.20^{+34.17}_{-27.51}$
log $n_{\rm ICM}$ (cm^{-3})
$F_{\rm V}$
$\sigma_{\rm cl}$ (km/s)
$v_{\rm cl}$ (km/s)
Δv (km/s)

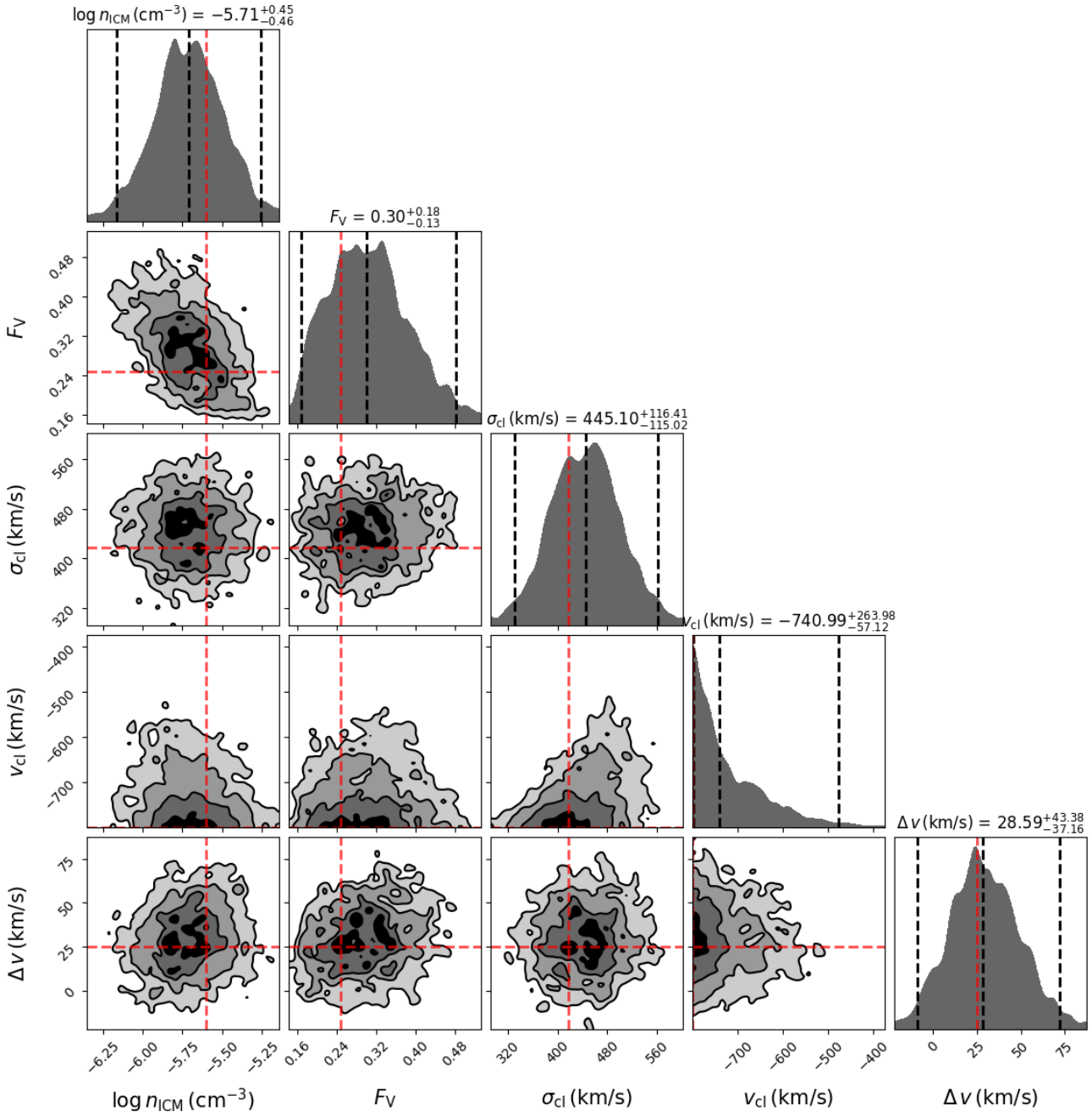
log n_{ICM} (cm^{-3}) = $-5.71^{+0.45}_{-0.46}$
F_V = $0.30^{+0.18}_{-0.13}$
σ_{cl} (km/s) = $445.10^{+116.41}_{-115.02}$
v_{cl} (km/s) = $-740.99^{+263.98}_{-57.12}$
Δv (km/s) = $28.59^{+43.38}_{-37.16}$
log n_{ICM} (cm^{-3})
F_V
σ_{cl} (km/s)
v_{cl} (km/s)
Δv (km/s)

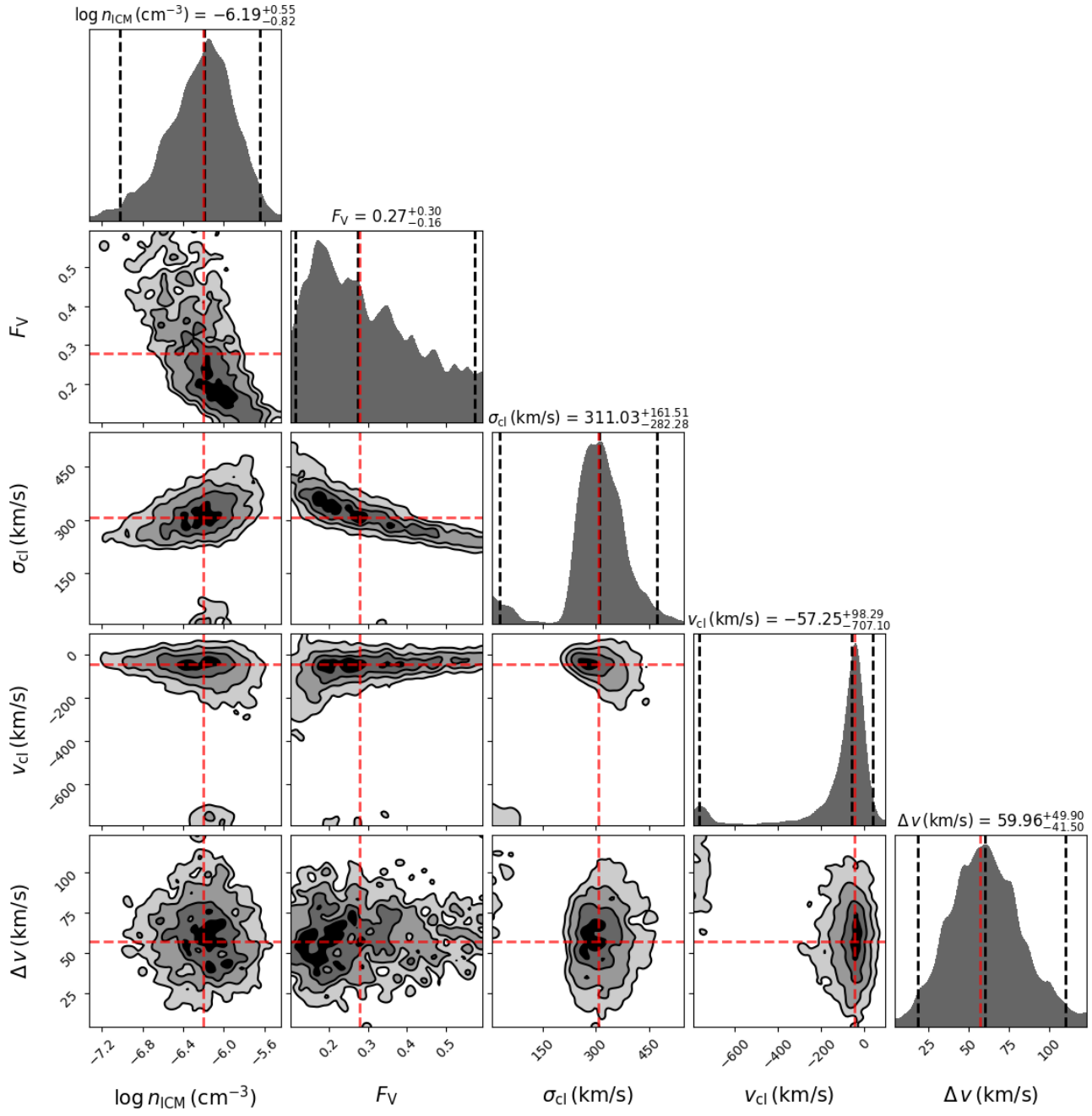

Figure A1. Joint and marginal posterior probability distributions of the multiphase, clumpy model parameters for all fifteen representative Lyα spectra derived from nested sampling. The vertical black dashed lines indicate the [2.5%, 50%, 97.5%] quantiles (i.e., 2-σ confidence intervals). The vertical red dashed lines indicate the locations of the maximum posterior probability.